ASME/2000 -Trib-61

A Paper Entitled

Fretting Stresses in Single Crystal Superalloy Turbine Blade Attachments

Submitted for presentation in the

International Joint Tribology Conference
Sponsored by ASME International and STLE
October 1-4, 2000
Seattle, Washington

And for publication in the ***ASME Journal of Tribology***

By

Nagaraj K. Arakere
Associate Professor
Mechanical Engineering Department
University of Florida
Gainesville, FL 32611-6300
(352) 392-0856: Tel; (352) 392-1071: Fax
nagaraj@ufl.edu

and

Gregory Swanson
NASA George C. Marshall Space Flight Center
ED22/Strength Analysis Group
MSFC, Alabama-35812

Fretting Stresses in Single Crystal Superalloy Turbine Blade Attachments

ABSTRACT

Single crystal nickel base superalloy turbine blades are being utilized in rocket engine turbopumps and turbine engines because of their superior creep, stress rupture, melt resistance and thermomechanical fatigue capabilities over polycrystalline alloys. Currently the most widely used single crystal nickel base turbine blade superalloys are PWA 1480/1493 and PWA 1484. These alloys play an important role in commercial, military and space propulsion systems. High Cycle Fatigue (HCF) induced failures in aircraft gas turbine and rocket engine turbopump blades is a pervasive problem. Blade attachment regions are prone to fretting fatigue failures. Single crystal nickel base superalloy turbine blades are especially prone to fretting damage because the subsurface shear stresses induced by fretting action at the attachment regions can result in crystallographic initiation and crack growth along octahedral planes. Furthermore, crystallographic crack growth on octahedral planes under fretting induced mixed mode loading can be an order of magnitude faster than under pure mode I loading.

This paper presents contact stress evaluation in the attachment region for single crystal turbine blades used in the NASA alternate Advanced High Pressure Fuel Turbo Pump (HPFTP/AT) for the Space Shuttle Main Engine (SSME). Single crystal materials have highly orthotropic properties making the position of the crystal lattice relative to the part geometry a significant factor in the overall analysis. Blades and the attachment region are modeled using a large-scale 3D finite element (FE) model capable of accounting for contact friction, material orthotrophy, and variation in primary and secondary crystal orientation. Contact stress analysis in the blade attachment regions is presented as a function of coefficient of friction and primary and secondary crystal orientation. Stress results are used to discuss fretting fatigue failure analysis of SSME blades. Attachment stresses are seen to reach peak values at locations where fretting cracks have been observed. Fretting stresses at the attachment region are seen to vary significantly as a function of crystal orientation. Attempts to adapt techniques used for estimating fatigue life in the airfoil region, for life calculations in the attachment region, are presented. An effective model for predicting crystallographic crack initiation under mixed mode loading is required for life prediction under fretting action.

Key Words

Fretting, Fatigue, High Cycle Fatigue (HCF), Single crystals, Crystal orientation, Nickel-base superalloys, Face Centered Cubic (FCC), Turbine blades, Blade attachments

Introduction

Fretting fatigue failure of mechanical components has gradually come to be recognized as a failure mode of major importance. The presence of fretting in conjunction with a mean stress in the body of a component can lead to a marked reduction in high cycle fatigue (HCF) life, sometimes by a factor as great as 10 [1]. Fretting occurs when assemblies of components such as blade and disk attachment surfaces, bolt flanges, snap fit areas, and other clamped members are subjected to vibration, resulting in contact damage. The combined effects of corrosion, wear, and fatigue phenomena at the fretting contact facilitates the initiation and subsequent growth of cracks, ultimately leading to failure. Single crystal nickel base superalloy turbine blades are especially prone to fretting damage because the subsurface shear stresses induced by fretting action at the attachment regions can result in crystallographic initiation and crack growth along octahedral planes.

Single crystal materials have highly orthotropic properties making the position of the crystal lattice relative to the part geometry a significant factor in the overall analysis. Study of failure modes of single crystal turbine blades therefore has to account for material orthotrophy and variations in crystal orientation. HCF induced failures in aircraft gas-turbine engines are a pervasive problem affecting a wide range of components and materials. HCF accounts for 24% of component failures in gas turbine aircraft engines, of which blade failures account for 40% [2]. Estimation of blade fatigue life, therefore, represents an important aspect of durability assessment. The modified Goodman approach currently used for life assessment does not address important factors that affect High Cycle Fatigue (HCF) such as fretting and/or galling surface damage, and interaction with Low Cycle Fatigue (LCF) [2]. Designing to resist fretting fatigue has proven to be a difficult task. The fretting fatigue process is affected by a large number of variables, perhaps by as many as fifty [3]. For polycrystalline materials the critical primary variables are thought to be the coefficient of friction, the slip amplitude, and the contact pressure at the fretting interface [1]. However, for single crystal nickel superalloys, studying the impact of fretting requires consideration of additional variables. The crack initiated by fretting action can be crystallographic or noncrystallographic depending on the interaction between the point-source defect species (carbides, micropores and eutectics) with the effects of environment, temperature and stress [4]. The impact of fretting on relationships between macroscopic fracture details and the parameters that are used to describe fatigue crack growth is essential. Understanding the effects of fretting damage on HCF life of single crystal nickel superalloy components is critical to lay a foundation for a mechanistic based life prediction system.

Turbine blades and vanes, used in aircraft and rocket engines, are probably the most demanding structural applications for high temperature materials [5] due to the combination of high operating temperature, corrosive environment, high monotonic and cyclic stresses, long expected component lifetimes, and the enormous consequence of structural failure. Directionally solidified (DS) columnar-grained and single crystal superalloys have the highest elevated-temperature capabilities of any superalloys. As the understanding of alloying and microstructural control (i.e., directional solidification) has improved, the maximum use temperatures of Ni-base superalloys has increased to levels in excess of 90% of their melting temperatures ($T/T_m = 0.9$). Directional solidification is used to produce a single crystal [6] with the <001> low modulus orientation parallel to the growth direction. The secondary direction normal to the growth direction, which is typically referenced to a line parallel to the blade attachment, is random if a grain selector is used to form the single crystal. Both the primary and secondary crystal orientations, though, can be selected if seeds are used to

generate the single crystal. However, in most cases, grain selectors are used to produce the desired <001> growth direction. In this case, the secondary orientations of the single crystal components are determined but not controlled. Initially, control of the secondary orientation was not considered necessary [7]. However, recent reviews of space shuttle main engine (SSME) turbine blade lifetime data has indicated that secondary orientation has a significant impact on high cycle fatigue resistance [8,9,10].

Currently the most widely used single crystal nickel base turbine blade superalloys are PWA 1480, PWA 1484, RENE' N-5 and CMSX-4. PWA 1480 will be used in the NASA SSME alternate turbopump. These alloys play an important role in commercial, military and space propulsion systems [4]. Military gas turbine mission profiles are characterized by multiple throttle excursions associated with maneuvers such as climb, intercept and air-to-air combat. This mission shifts attention somewhat to fatigue and fracture considerations associated with areas below the blade platform, which contain various stress risers in the form of buttresses and attachments [4]. The gas turbine industry is moving toward a design philosophy that stresses damage tolerance, structural integrity and threshold based designs, which has prompted the study of micromechanics of fretting fatigue and other events that affect HCF life.

Numerous analytical and experimental studies have been conducted on fretting fatigue damage in polycrystalline alloys. Some representative examples are by Hills and Newell [1], Giannokopoulos and Suresh [11], Swolwinsky and Farris [12], Attia and Waterhouse [13], Hoeppner [14], Vingsbo and Soderberg [15], and Ruiz, et al [16]. Studies on mechanics of fretting fatigue in single crystal superalloys are almost nonexistent. This paper presents an investigation of fretting stresses in single crystal superalloy turbine blades in the blade-disk attachment regions. Large-scale finite element models of are used to predict stresses in the airfoil and blade attachment regions. Several fatigue damage parameters based on shear and normal stresses acting on various slip planes for FCC crystals are evaluated. Blade stress response is presented as a function of primary and secondary crystallographic orientation.

Deformation Mechanisms in FCC Single Crystals

Nickel based single-crystal material such as PWA1480 and PWA1484 are precipitation strengthened cast single grain superalloys based on the Ni-Cr-Al system. The microstructure consists of approximately 60% to 70% by volume of γ' precipitates in a γ matrix. The γ' precipitate, based on the intermetallic compound Ni_3Al, is the strengthening phase in nickel-base superalloys and is a Face Centered Cubic (FCC) structure. The γ' precipitate is suspended within the γ matrix also has a FCC structure and is comprised of nickel with cobalt, chromium, tungsten and tantalum in solution.

Deformation mechanisms in single crystals are primarily dependent on microstructure, orientation, temperature, and crystal structure. The operation of structures at high temperature places additional materials constraints on the design that are not required for systems that operate at or near room temperatures. In general, materials become weaker with increasing temperature due to thermally activated processes, such as multiple slip and cross-slip. At temperatures in excess of approximately half the homologous temperature (the ratio of the test temperature to the melting point, = T/T_m), diffusion controlled processes (e.g., recovery, recrystallization, dislocation climb and grain growth) become important, which results in further reductions in strength. Slip in metal crystals often occurs

on planes of high atomic density in closely packed directions. The 4 octahedral planes corresponding to the high-density planes in the FCC crystal have 3 primary slip directions (easy-slip) resulting in 12 independent primary <110> {111} slip systems. The 4 octahedral slip planes also have 3 secondary slip directions resulting in 12 independent secondary <112> {111} slip systems. In addition, the 3 cube slip planes have 2 slip directions resulting in 6 independent <110> {100} cube slip systems. Thus there are 12 primary and 12 secondary slip systems associated with the 4 octahedral planes and 6 cube slip systems with the 3 cube planes, for a total of 30 slip systems [10]. At high temperatures, slip has been observed in non-close-pack directions on the octahedral plane, and on the cube plane, in FCC crystals. Table 1 shows the 30 possible slip systems in a FCC crystal [17]. Elastic response of FCC crystals is obtained by expressing Hooke's law for materials with cubic symmetry.

Shear stresses associated with the 30 slip systems are denoted by $\tau^1, \tau^2, \ldots, \tau^{30}$. The shear stresses on the 24 octahedral slip systems are given by [17],

$$\begin{Bmatrix} \tau^1 \\ \tau^2 \\ \tau^3 \\ \tau^4 \\ \tau^5 \\ \tau^6 \\ \tau^7 \\ \tau^8 \\ \tau^9 \\ \tau^{10} \\ \tau^{11} \\ \tau^{12} \end{Bmatrix} = \frac{1}{\sqrt{6}} \begin{bmatrix} 1 & 0 & -1 & 1 & 0 & -1 \\ 0 & -1 & 1 & -1 & 1 & 0 \\ 1 & -1 & 0 & 0 & 1 & -1 \\ -1 & 0 & 1 & 1 & 0 & -1 \\ -1 & 1 & 0 & 0 & -1 & -1 \\ 0 & 1 & -1 & -1 & -1 & 0 \\ 1 & -1 & 0 & 0 & -1 & -1 \\ 0 & 1 & -1 & -1 & 1 & 0 \\ 1 & 0 & -1 & -1 & 0 & -1 \\ 0 & -1 & 1 & -1 & -1 & 0 \\ -1 & 0 & 1 & -1 & 0 & -1 \\ -1 & 1 & 0 & 0 & 1 & -1 \end{bmatrix} \begin{Bmatrix} \sigma_{xx} \\ \sigma_{yy} \\ \sigma_{zz} \\ \sigma_{xy} \\ \sigma_{zx} \\ \sigma_{yz} \end{Bmatrix}, \quad \begin{Bmatrix} \tau^{13} \\ \tau^{14} \\ \tau^{15} \\ \tau^{16} \\ \tau^{17} \\ \tau^{18} \\ \tau^{19} \\ \tau^{20} \\ \tau^{21} \\ \tau^{22} \\ \tau^{23} \\ \tau^{24} \end{Bmatrix} = \frac{1}{3\sqrt{2}} \begin{bmatrix} -1 & 2 & -1 & 1 & -2 & 1 \\ 2 & -1 & -1 & 1 & 1 & -2 \\ -1 & -1 & 2 & -2 & 1 & 1 \\ -1 & 2 & -1 & -1 & -2 & -1 \\ -1 & -1 & 2 & 2 & 1 & -1 \\ 2 & -1 & -1 & -1 & 1 & 2 \\ -1 & -1 & 2 & 2 & -1 & 1 \\ 2 & -1 & -1 & -1 & -1 & -2 \\ -1 & 2 & -1 & -1 & 2 & 1 \\ 2 & -1 & -1 & 1 & -1 & 2 \\ -1 & 2 & -1 & 1 & 2 & -1 \\ -1 & -1 & 2 & -2 & -1 & -1 \end{bmatrix} \begin{Bmatrix} \sigma_{xx} \\ \sigma_{yy} \\ \sigma_{zz} \\ \sigma_{xy} \\ \sigma_{zx} \\ \sigma_{yz} \end{Bmatrix} \quad (1)$$

And the shear stresses on the 6 cube slip systems are

$$\begin{Bmatrix} \tau^{25} \\ \tau^{26} \\ \tau^{27} \\ \tau^{28} \\ \tau^{29} \\ \tau^{30} \end{Bmatrix} = \frac{1}{\sqrt{2}} \begin{bmatrix} 0 & 0 & 0 & 1 & 1 & 0 \\ 0 & 0 & 0 & 1 & -1 & 0 \\ 0 & 0 & 0 & 1 & 0 & 1 \\ 0 & 0 & 0 & 1 & 0 & -1 \\ 0 & 0 & 0 & 0 & 1 & 1 \\ 0 & 0 & 0 & 0 & -1 & 1 \end{bmatrix} \begin{Bmatrix} \sigma_{xx} \\ \sigma_{yy} \\ \sigma_{zz} \\ \sigma_{xy} \\ \sigma_{zx} \\ \sigma_{yz} \end{Bmatrix} \quad (2)$$

Shear strains (engineering) on the 30 slip systems are calculated using similar kinematic relations. The stresses (σ_{xx}, σ_{yy}, ..., σ_{yz}) must be expressed in the material or the crystal coordinate system, i.e., the x, y, and z coordinate axes are parallel to the edges of the FCC crystal.

Fretting Fatigue Crack Initiation and Crack Growth in Nickel-Base Superalloys

Crack initiation in Ni-base superalloys fall into two broad classifications, crystallographic and noncrystallographic. The interaction between the effects of environment, temperature and stress

intensity determines which point-source defect species initiates a crystallographic or noncrystallographic fatigue crack [4]. At low temperature (<427 C) and stress conditions crystallographic initiation appears to be the most prevalent mode. At moderately high temperature (above 593C) initiation at TaC carbides predominates over occasional (111) eutectic origins. The subsurface shear stresses induced by fretting action can result in crystallographic initiation of failure, as seen in Fig. 1, which shows a subsurface fatigue crack emanating from a carbide (TaC) in a turbine blade attachment (PWA1422, a columnar grain Ni-base superalloy) and propagating along octahedral (111) planes [4]. Fretting fatigue at low slip amplitudes that induces little or no surface damage can result in greatly reduced fatigue life with accelerated subsurface crystallographic crack initiation, akin to subsurface shear stress induced rolling bearing fatigue. An example of this phenomenon is seen in Fig. 2, which details the underside view of a single crystal Ni (PWA1480) turbine blade platform tip fretting failure at the contact where a centrifugal damper impinged the blade platform [18]. The damper (or fret pin) was subjected to an alternating compressive load generating subsurface shear stresses. The fretting fatigue crack initiation was clearly subsurface, propagating along intersecting (111) crystallographic planes until breaking out to the surface. The piece was subsequently ejected. An identical scenario occurred with the impinging damper. The damper was quite small and cast in a very coarse grained form such that the contact point was a single large grain. It too exhibited a subsurface crystallographic shear fatigue crack initiation/propagation on multiple intersecting octahedral planes leading to a pyramidal "hole" in the component as the "chip" was ejected.

The fatigue crack growth (FCG) behavior of single crystal nickel superalloys is governed by a complex interaction between the operative deformation mechanism, stress intensity, and environmental conditions. The FCG behavior is determined by the operative microscopic fracture mode. As a result of the two phase microstructure present in single crystal nickel alloys a complex set of fracture mode exists based on the dislocation motion in the matrix (γ) and precipitate phase (γ'). Telesman and Ghosn [19] have observed the transition of fracture mode as a function of stress intensity (K) in PWA1480 at room temperature. They also noted that, K_{rss}, the resolved shear stress intensity parameter on the 12 primary slip planes predicted the crack zigzag behavior caused by fracture mode transitions. Deluca and Cowles [20] have observed the fracture mode transition that is environmentally dependent (presence of high-pressure hydrogen). The resolved shear stresses and not the maximum principal stresses govern failure on the (111) octahedral slip planes. However stresses normal to the plane (mode I component) are thought to play some role in the failure process. Crystallographic crack growth along (111) planes under mixed mode loading can be an order of magnitude faster than under pure mode I loading [21]. These results have important implications on fretting fatigue. Since fretting action results in mixed mode loading this can result in crystallographic initiation along (111) slip planes (Fig. 1) and rapid crack growth under loads lower than that expected under mode I loading.

Effect of Crystal Orientation on Fatigue Life

Single crystal materials have highly orthotropic properties making the position of the crystal lattice relative to the part geometry a significant factor in the overall analysis. For example, the elastic or Young's modulus (E) is a strong function of crystal orientation over the standard stereographic triangle, given by Eq. (3) [22].

$$E^{-1} = S_{11} - [2(S_{11} - S_{12}) - S_{44}][\cos^2\phi(\sin^2\phi - \sin^2\theta\cos^2\phi\cos^2\theta)] \qquad (3)$$

Where θ is the angle between the growth direction and <001> and ϕ is the angle between the <001> - <110> boundary of the triangle. The terms S_{11}, S_{12} and S_{44} are the elastic compliances. In general, the elastic properties are insensitive to composition and values for pure Ni are a good approximation of the values for even the most highly alloyed Ni-base superalloys.

Strain controlled LCF tests conducted at 1200 F in air for PWA1480/1493 uniaxial smooth specimens, for four different orientations, is shown in Table 2 [9]. The four specimen orientations are <001> (5 data points), <111> (7 data points), <213> (4 data points), and <011> (3 data points), for a total of 19 data points. Figure 3 shows the plot of strain range vs. Cycles to failure. A wide scatter is observed in the data with poor correlation for a power law fit. Table 3 shows the fatigue parameters such as $\Delta\tau_{max}$, $\Delta\sigma_{max}$, $\Delta\varepsilon$, $\Delta\gamma$, etc computed on the 30 slip systems. The procedure for obtaining values shown in Table 3 is explained in greater detail by Arakere and Swanson [9]. Other fatigue parameters used in polycrystalline material were also evaluated in reference [9], besides $\Delta\tau_{max}$. Figure 4 shows that the maximum shear stress amplitude $\Delta\tau_{max}$ plotted against cycles to failure, N, has a good correlation for a power law fit. The power law curve fit is shown by Eq. (4).

$$\Delta\tau_{max} = 397{,}758\ N^{-0.1598} \qquad (4)$$

The correlation for $[\Delta\tau_{max}]$ would be better if some of the high stress data points are corrected for inelastic effects. It must be noted that Eq. (4) is only valid for PWA1480/1493 material at 1200F. Since the deformation mechanisms in single crystals are controlled by the propagation of dislocations driven by shear the $[\Delta\tau_{max}]$ might indeed be a good fatigue failure parameter to use for crystallographic cracking. However, this parameter must be verified for a wider range of R-values and specimen orientations, and also at other temperatures and environmental conditions. Equation (4) will be used to calculate fatigue life at a critical blade tip location for the SSME turbine blade.

Fatigue Failure in SSME HPFTP/AT Single Crystal Turbine Blades

Turbine blades used in the alternate high-pressure fuel turbopump (HPFTP/AT) for the NASA SSME are fabricated from single crystal nickel PWA1480/1493 material. Many of these blades have failed during testing due to fretting/galling fatigue cracks in the attachment regions and the initiation and propagation of fatigue cracks from an area of high concentrated stress at the blade tip leading edge. The subsequent investigation into the blade tip cracking failure provided insight into areas where the robustness of the design could be improved to reduce the potential for failure. During the course of the investigation an interesting development was brought to light. When the size of the fatigue cracks for the population of blades inspected was compared with the secondary crystallographic orientation β a definite relationship was apparent as shown in Fig. 5 [8, 23]. Secondary orientation does appear to have considerable influence over whether a crack will initiate and arrest or continue to grow until failure of the blade airfoil occurs. Figure 5 reveals that for β = 45+/- 15 degrees tip cracks arrested after some growth or did not initiate at all. This suggests that perhaps there are preferential β orientations for which crack growth is minimized at the blade tip.

In an attempt to understand the effect of crystal orientation on blade stress response at the blade tip and in the attachment regions a detailed three-dimensional finite element (FE) model capable of accounting for primary and secondary crystal orientation variation was constructed [10, 24].

Description of the Blade Finite Element (FE) Model

The blade FE model is described in detail by the present authors in reference [9], which deals with the effects of crystal orientation on blade fatigue life. A brief description of the model is repeated here for completeness. The Alternate High Pressure Fuel Turbo Pump (HPFTP/AT) first stage blade ANSYS FE model was constructed from a large 3D cyclic symmetry model that includes the first and second stage blades and retainers, interstage spacer, disk and shaft, and the disk covers [10]. The FE models are geometrically nonlinear due to the contact surfaces between the separate components. The element type used for the blade material is the ANSYS SOLID45, an 8-noded 3D solid isoparametric element. Anisotropic material properties are allowed with this element type. The FE model of the first stage turbine blade with the frequently observed blade tip cracking problem is shown in Fig. 6. Figure 6 also shows the material coordinate system, which is referenced, to the blade casting coordinate system.

To examine a wide range of primary and secondary variations in crystal orientation, 297 material coordinate systems were generated for this study. The primary and secondary crystallographic orientation is shown in Fig. 7 [8]. Figure 8 shows the distribution of the 297 different material coordinate systems within the allowed 15-degree maximum deviation from the casting axis. The secondary repeats after 90 degrees, so only 0 to 80 degrees needed to be modeled. The two angles, Δ and Γ, locate the primary material axis relative to the casting axis, and the third angle, β, is the clocking of the secondary material axis about the primary material axis.

The loading conditions represent full power mainstage operation of the Space Shuttle Main Engine, referred to as 109% RPL SL (Rated Power Level Service Life). The shaft speed is 37,355 rpm, the airfoil temperature is approximately 1200 F, forces representing the blade damper radial sling load are applied to the blade platform, and aerodynamic pressures are applied to the blade surfaces and internal core.

The connection between the blade and disk are modeled with ANSYS COMBIN40 elements, for cases where the coefficient of friction between the blade-disk attachments was ignored. These elements have one degree of freedom at each node. The nodal motion in that degree of freedom sets the separation or contact of these elements only. This element does not have the capability for friction tangent to the contact surface.

To account for coefficient of friction at the blade attachment regions, the COMBIN40 element was replaced with CONTAC52 type elements. The CONTAC52 element has 3 degrees of freedom at each node. Coefficient of friction at the contact is allowed, thus developing tangential traction forces. The relative position and motion of the end nodes are used to define displacement and reaction force magnitude and direction at the contact. For FE models including friction at the attachment regions,

Post processing of the 297 FE output files represented a considerable amount of work. Two FORTRAN programs, developed at MSFC, were employed for this effort. The first strips the element results from the coded binary output files and places them into ASCII text files. The second program processes the ASCII files to calculate averaged nodal results, the resolved shear stresses and strains and the normal stresses and strains in the single crystal material coordinate system. Fatigue parameters chosen for study are then calculated and sorted based on user set

criteria. Postprocessing of the friction data was performed by constructing a local coordinate system with one axis in the tangential direction of contact slip on the blade attachment (Fig. 14). An ANSYS batch-postprocessing routine was written to output tabulated results for selected nodes in the attachment.

Effect of Crystal Orientation on Blade Tip Stress Response

Effect of crystal orientation on stress response at the blade tip critical point is discussed first, followed by a discussion of stresses in the blade attachment region. The crack location and orientation at the critical blade tip location is shown in Fig. 5. Stress response at the blade tip as a function of crystal orientation is discussed in greater detail in reference [9].

Fatigue life estimation of single crystal turbine blade components represents an important aspect of durability assessment. Towards identifying a fatigue damage parameter for single crystal blade material, several fatigue failure criteria used for polycrystalline material subjected to multiaxial states of fatigue stress were evaluated for single crystal material by Arakere and Swanson [9]. They are outlined here briefly to facilitate comparisons with fatigue in contact locations.

Turbine blade material is subjected to large mean stresses from the centrifugal stress field. High frequency alternating fatigue stresses are a function of the vibratory characteristics of the blade. Kandil, et al [25] presented a shear and normal strain based model, shown in Eq. 5, based on the critical plane approach, which postulates that cracks initiate and grow on certain planes and that the normal strains to those planes assist in the fatigue crack growth process. In Eq. (5) γ_{max} is the max shear strain on the critical plane, ε_n the normal strain on the same plane, S is a constant, and N is the cycles to initiation.

$$\gamma_{\max} + S\,\varepsilon_n = f(N) \tag{5}$$

Socie, et al [26] presented a modified version of this theory shown in Eq. (6), to include mean stress effects. Here the maximum shear strain amplitude ($\Delta\gamma$) is modified by the normal strain amplitude ($\Delta\varepsilon$) and the mean stress normal to the maximum shear strain amplitude (σ_{no}). These observations are similar to FCG on octahedral planes for single crystals.

$$\frac{\Delta\gamma}{2} + \frac{\Delta\varepsilon_n}{2} + \frac{\sigma_{no}}{E} = f(N) \tag{6}$$

Fatemi and Socie [27] have presented an alternate shear based model for multiaxial mean-stress loadings that exhibit substantial out-of-phase hardening, shown in Eq. (7). This model indicates that no shear direction crack growth occurs if there is no shear alternation.

$$\frac{\Delta\gamma}{2}\left(1 + k\frac{\sigma_n^{\max}}{\sigma_y}\right) = f(N) \tag{7}$$

Smith, Watson, and Topper [28] proposed a uniaxial parameter to account for mean stress effects which was modified for multiaxial loading, shown in Eq. (8), by Bannantine and Socie [29]. Here

the maximum principal strain amplitude is modified by the maximum stress in the direction of maximum principal strain amplitude that occurs over one cycle.

$$\frac{\Delta\varepsilon_1}{2}(\sigma^{\max}) = f(N) \tag{8}$$

Equation 8 has been used successfully for prediction of crack initiation in fretting fatigue, for aluminum and titanium polycrystalline alloys [12]. The polycrystalline failure parameters based on equations (5-8) was applied for single crystal uniaxial LCF test data, shown in Table 2, by evaluating the fatigue damage parameters on all of the 30 slip systems [9, 10]. However, the most effective fatigue damage parameter was found to be maximum shear stress amplitude $\Delta\tau_{max}$ shown in Fig. 4.

Variation of crystal orientation on stress response at the blade tip critical point prone to cracking (tip point on inside radius) was examined by analyzing the results from the 297 FE model runs. The FE node at the critical point was isolated and critical failure parameter value ($\Delta\tau_{max}$) computed on the 30 slip systems. A contour plot of $\Delta\tau_{max}$ was generated as a function of primary and secondary orientation, shown in Fig. 9. The contour plot clearly shows a minimum value for $\Delta\tau_{max}$ for secondary orientation of β = 50 deg and primary orientation designated by cases 5 and 20. Case 5 corresponds to a primary orientation of Δ = 0 deg and Γ = 7.5 degree. Case 20 corresponds to a primary orientation of Δ = 5.74 deg and Γ = 13.86 degree. Using the fatigue life equation based on the $\Delta\tau_{max}$ curve fit of LCF test data (Eq. 4) we can obtain a contour plot of dimensionless life at the critical point as a function of primary and secondary orientation, as shown in Fig. 10. The maximum life is again obtained for β = 50 deg, and Δ = 0 deg and Γ = 7.5 deg, and Δ = 5.74 deg and Γ = 13.86 deg. The optimum value of secondary orientation β = 50 deg. corresponds very closely to the optimum value of β indicated in Fig. 5. *This demonstrates that control of secondary and primary crystallographic orientation has the potential to significantly increase a component's resistance to fatigue crack growth without adding additional weight* (for the airfoil region).

Stress Response in the Attachment Region (Frictionless Contact)

The 297 FE models representing 33 variations (cases) in primary crystal orientation and 9 variations in the secondary orientation were run for frictionless contacts at the blade attachments. Blade loading conditions were kept constant while the crystal orientation was varied. Figure 11 shows representative stress plots for the blade attachment region. The critical point with the most severe contact stresses is shown in Fig. 12. Fretting damage in the attachment regions is highlighted in Figs. 13-14. Effects of variation of primary and secondary orientation on stress response are studied for this critical region. Figures 15-16 show contour plots of $\Delta\tau_{max}$ and $\tau_{max} * \Delta\gamma/2$, as a function of primary and secondary orientation. The crystal orientation does not appear to have any discernable correlation at the contact point for these parameters. Figure 17 shows a contour plot of ($\sigma_{max}\ \Delta\varepsilon/2$, Eq. 8) as a function of primary and secondary orientation. The secondary orientation does appear to have an optimum value of about 55 degrees. Szolwinski and Farris [12] have used Eq. (8) successfully as a fretting damage parameter for polycrystalline alloys. For single crystal material, however, the fretting damage parameters need to be evaluated in greater detail. A simpler geometry such as a cylindrical fret pin made of polycrystalline material contacting a flat plate made of single crystal material with a specific crystal orientation would be amenable to an analytical

solution. Surface and subsurface stresses at the contact can then be examined in detail, and fretting damage parameters evaluated, as a function of crystal orientation, coefficient of friction, slip amplitude, loads, etc.

Figures 1 and 2 illustrate that subsurface shear stresses from fretting action, at low or even zero slip amplitude, can induce subsurface crystallographic crack initiation, with stage I-fatigue cracks propagating outward to the surface. No crack involvement of the fretted surface occurs and negligible surface damage is noted at the contact surfaces. Clearly, an effective model for predicting crystallographic crack initiation under mixed mode loading is required for life prediction under fretting action.

This study shows that stress at the attachment region varied significantly as a function of crystal orientation alone, from τ_{max}= 60 ksi to τ_{max}= 130 ksi. This indicates that by selecting the appropriate crystal orientation, for specified geometry and loading, it may be possible to optimize blade structural integrity.

Stress Response in the Attachment Region Including Contact Friction

The presence of friction results in the development of traction forces at the fretting contact. Evaluation of the contact forces and the resulting contact stresses at the interface require careful analysis of the interaction between the contacting surfaces and applied loads. To study the effect of variation of friction coefficient at the contact, and variation of primary and secondary crystal orientations, 18 FE model runs were completed. The 18 FE models comprised of 3 primary orientations (cases 0, 5 and 30), 2 secondary orientations (β = 0 and 50 deg.), and 3 values for coefficient of friction (μ = 0, 0.3, 0.7). Figure 12 shows representative contact stress results in the critical attachment region. Blade loading is kept constant for all 18 cases. Figure 18 shows contour plots of tangential normal stress, σ_X, at the contact surface. The X coordinate is in the direction of slip, as shown in Fig. 12. The tangential normal stress is of practical interest because cracks are thought to initiate at locations where σ_X reaches a maximum tensile value. The maximum value of tangential normal stress, σ_X, reached in the contact zone is listed in Table 4 for all the 18 cases. It is seen that σ_X increases with μ. σ_X is also seen to vary considerably with variations in primary and secondary orientation. Since the component stiffness varies with crystal orientation the stress distribution is also expected to vary, under constant loading. Minimum values of σ_X are reached for case 30 and β=0 [(84.3 ksi, μ=0), (89.9 ksi, μ=0.3), (97.7 ksi, μ=0.7)] indicating that perhaps key design parameters can be optimized for specific blade geometry and loading. Additional fretting damage parameters need to be examined, for design optimization possibilities.

The frictional contact study showed that both σ_X and τ_{max} stresses at the attachment region varied by about 20%, as a function of crystal orientation alone. For instance, the σ_X variations (Table 4) as a function of crystal orientation alone are 84.3 – 108.6 ksi for μ = 0, 89.9 – 114.4 ksi for μ = 0.3, and 97.7 – 122.6 ksi for μ = 0.7. The variations would have been larger if peak variations due to crystal orientation were realized. It appears that if case 25 with β=30° was compared with case 17 at β=0° or, β=20° stress variations due to crystal orientation would have been considerably larger than 20%.

Figures 13 and 14 show representative fretting/galling induced cracks in the blade attachment region for HPFTP/AT first stage blades. Region shown in Fig. 13 is on the suction side, trailing

edge of the blade. Several arrest marks are also visible. The blade crystal orientation is $\Delta = -6.7^{\circ}$, $\gamma = 11.3^{\circ}$, $\beta = 4.2^{\circ}$. Figure 14 shows fretting/galling induced cracking showing multiple origins with stage II cracks. The crystal orientation for this blade is $\Delta = -2^{\circ}$, $\gamma = 3^{\circ}$, $\beta = 7^{\circ}$. Many blades in different engine units exhibited similar blade attachment cracks. In the blade casting process, the secondary crystal orientation is not controlled, while the primary crystal orientation is controlled to within 15°. A systematic investigation of severity of fretting/galling induced attachment cracks, similar to study shown in Fig. 5 for blade tip cracking, has to be done to discern relationships between fretting damage and crystal orientation. Tolerance in clearance between the blade and disk attachment surfaces also plays an important role in the contact stress distribution. The analysis results presented are for nominal clearances between mating parts.

Conclusions

Three dimensional finite element stress analysis of HPFTP/AT SSME single crystal turbine blades subjected to rotational, aerodynamic, and thermal loads is presented. Stress response at the blade tip and attachment regions are presented as a function of primary and secondary crystal orientation. 297 FE models are analyzed to study a wide range of variation in crystal orientation. For the blade tip location, the maximum shear stress amplitude [$\Delta\tau_{max}$] on the 30 slip systems was found to be an effective fatigue failure criterion, based on the curve fit between $\Delta\tau_{max}$ and LCF data at 1200F for PWA1480/1493. Variation of $\Delta\tau_{max}$ as a function of crystal orientation at the blade tip reveals that control of secondary and primary crystallographic orientation has the potential to significantly increase a component's resistance to fatigue crack growth without adding additional weight or cost. Current seeding techniques used in the single crystal casting process can readily achieve the degrees of control in primary and secondary crystallographic orientation required. Fretting contact stresses are presented for the attachment region. Attachment stresses are seen to reach peak values at locations where fretting cracks have been observed. For frictionless contact, stress at the attachment region varied significantly as a function of crystal orientation alone, from τ_{max} =60 ksi to τ_{max} = 130 ksi, under constant loading conditions. Attachment stresses varied significantly for models that included coefficient of friction at the contact. The tangential normal stress σ_X increased with increasing coefficient of friction at the critical contact location. This might be of practical interest since cracks are thought to initiate at locations where σ_X reaches a maximum tensile value, for polycrystalline materials. The parameter $\Delta\tau_{max}$, which showed a definite correlation with crystal orientation at the blade tip, appears to have no discernable correlation at the critical contact region. The damage parameter $\sigma_{max}\,\Delta\varepsilon/2$ appears to be correlated with the secondary orientation. Fretting damage parameters need to be evaluated in greater detail for single crystal materials.

Subsurface shear stresses induced by fretting action, at low or even zero slip amplitude, can induce subsurface crystallographic crack initiation, with no crack involvement of the fretted surface. An effective model for predicting crystallographic crack initiation under mixed mode loading is required for life prediction under fretting action. This will necessitate specialized testing to account for crystal orientation and mixed mode loading effects. One way to conduct these tests is to use Brazilian disk specimens as outlined by John, et al [21], to study mixed mode loading in single crystals. However, to study crystallographic crack initiation behavior, the disks would have to be tested without starter flaws, requiring high compressive loads and potential for failure at the loading points. One solution perhaps is to thin the disks at the center which necessitates lower compressive loads to initiate a crystallographic crack at the disk center.

Acknowledgements

The authors would like to thank the NASA/ASEE 1999 Summer Faculty Fellowship Program. The support from this program, administered by the University of Alabama in Huntsville, enabled the first author to perform part of this work at the NASA Marshall Space Flight Center, Huntsville, AL.

REFERENCES CITED

[1] *D. A. Hills and D. Nowell, Mechanics of Fretting Fatigue*, Kluwer, Deventer, 1994.

[2] B. A. Cowles, High cycle fatigue in aircraft gas turbines-an industry perspective, *International Journal of Fracture*, (1996) 1-16.

[3] J. Dombromirski, Variables of Fretting Process: Are There 50 of them? *Standardization of Fretting Fatigue Test Methods and Equipment*, ASTM, pp. 60-68, 1990.

[4] Deluca, D., Annis. C, "Fatigue in Single Crystal Nickel Superalloys"; Office of Naval Research, Department of the Navy FR23800, August 1995.

[5] C.T. Sims, "Superalloys: Genesis and Character", Superalloys – II, Eds., C.T. Sims, N.S. Stoloff and W.C. Hagel, Wiley & Sons, New York, New York, (1987), p. 1.

[6] F.L. VerSnyder and R.W. Guard, "Directional Grain Structure for High Temperature Strength", *Trans. ASM*, 52, (1960), p. 485.

[7] M. Gell and D.N. Duhl, "The Development of Single Crystal Superalloy Turbine Blades", Processing and Properties of Advanced High-Temperature Materials, Eds., S.M. Allen, R.M. Pelloux and R. Widmer, ASM, Metals Park, Ohio, (1986), p. 41.

[8] J. Moroso, "Effect of Secondary Orientation on Fatigue Crack Growth in Single Crystal Turbine Blades", M.S. Thesis, Mechanical Engineering Department, University of Florida, Gainesville, FL, May 1999.

[9] N. K. Arakere and G. Swanson, "Effect of Crystal Orientation on Fatigue Failure of Single Crystal Nickel Base Turbine Blade Superalloys," accepted for presentation in the ASME IGTI conference (May 8-11, 2000, Munich, Germany) and for publication in the *ASME Journal of Gas Turbines and Power*.

[10] N. K. Arakere and G. Swanson, "Fatigue Failure of Single Crystal Nickel Base Turbine Blade Superalloys," accepted for publication as a NASA Technical Paper.

[11] Giannokopoulos and S. Suresh, "3D Fretting Stresses," *Acta Materialia*, 1999.

[12] M. P. Szolwinski and T. N. Farris, "Mechanics of Fretting Fatigue Crack Formation," *Wear*, v 198, 1996, pp. 93-107.

[13] M. H. Attia and R. B. Waterhouse, Editors, Standardization of Fretting Fatigue Test Methods and Equipment, *ASTM* (04-011590-30), STP 1159, (1992)

[14] D. W. Hoeppner, Mechanisms of Fretting Fatigue and Their Impact on Test Methods Development, Standardization of Fretting Fatigue Test Methods and Equipment, ASTM, pp. 23-32, 1990.

[15] O. Vingsbo and D. Soderberg, On fretting maps, *Wear*, 126 (1988) 131-147.

[16] C. Ruiz, P. H. B. Boddington and K. C. Chen, An investigation of fatigue and fretting in a dovetail joint, *Experimental mechanics*, 24 (3) (1984) 208-217.

[17] Stouffer, D. C., and Dame, L. T., "Inelastic Deformation of Metals," John Wiley & Sons; 1996.

[18] Personal Communication with D. P. DeLuca, Pratt & Whitney, (Government Engines and Space Propulsion), Mechanics of Materials, West Palm Beach, FL.

[19] Telesman, J.; Ghosn, L, "The unusual near threshold FCG behavior of a single crystal superalloy and the resolved shear stress as the crack driving force," *Engineering Fracture Mechanics*, Vol. 34, No. 5/6, pp. 1183-1196, 1989.

[20] Deluca, D. P. and Cowles, B. A., "Fatigue and fracture of single crystal nickel in high pressure hydrogen", *Hydrogen Effects on Material Behavior*, Ed. By N. R. Moody and A. W. Thomson, TMS., Warrendale, PA, 1989.

[21] John, R., DeLuca, D. P., Nicholas, T., and Porter, J., "Near-threshold crack growth behavior of a single crystal Ni-base superalloy subjected to mixed mode loading," *Mixed-Mode Crack Behavior*, ASTM STP 1359, Editors. K. J. Miller and D. L. McDowell, Paper ID: 5017, November 1998.

[22] M. McLean, "Mechanical Behavior: Superalloys", Directionally Solidified Materials for High Temperature Service, *The Metals Society*, London, (1983), p. 151.

[23] Pratt and Whitney, "SSME Alternate Turbopump Development Program HPFTP Critical Design Review," P&W FR24581-1 December 23, 1996. NASA Contract NAS8-36801.

[24] Sayyah, T., "Alternate Turbopump Development Single Crystal Failure Criterion for High Pressure Fuel Turbopump First Stage Blades," Report No.: 621-025-99-001, NASA Contract NAS 8-40836, May 27, 1999.

[25] Kandil, F. A., Brown, M. W., and Miller, K. J., "Biaxial low cycle fatigue of 316 stainless steel at elevated temperatures," Book, pp. 203-210, Metals Soc., London, 1982.

[26] Socie, D. F., Kurath, P., and Koch,J., "A multiaxial fatigue damage parameter," presented at the Second International Symposium on Multiaxial Fatigue, Sheffield, U.K., 1985.

[27] Fatemi, A, Socie, D, "A Critical Plane Approach to Multiaxial Fatigue Damage Including Out-of-Phase Loading," *Fatigue Fracture in Engineering Materials*, Vol. 11, No. 3, pp. 149-165, 1988.

[28] Smith, K. N., Watson, P., and Topper, T. M., "A stress-strain function for the fatigue of metals," *Journal of Materials*, Vol. 5, No. 4, pp. 767-778, 1970.

[29] Banantine, J. A., and Socie, D. F., "Observations of cracking behavior in tension and torsion low cycle fatigue," presented at ASTM Symposium on low cycle fatigue – Directions for the future, Philadelphia, 1985.

LIST OF FIGURES

Fig. 1 A subsurface fretting fatigue crack emanating from a carbide in a turbine blade attachment (PWA1422) and propagating along octahedral (111) shear planes [4].

Fig. 2 Subsurface fretting fatigue crack initiation in a single crystal Ni turbine blade (platform tip) [18]

Fig. 3 Strain range Vs. Cycles to Failure for LCF test data (PWA1493 at 1200F)

Fig. 4 Shear Stress Amplitude [$\Delta\tau_{max}$] Vs. Cycles to Failure

Fig. 5 Secondary Crystallographic Orientation, β, Vs Crack Depth for the SSME AHPFTP 1st Stage Turbine Blade [8, 23]

Fig. 6. First Stage Turbine Blade FE Model and Casting Coordinate System

Fig. 7 Convention for Defining Crystal Orientation in Turbine Blades [8]

Fig. 8 33 primary crystallographic orientations (cases) and 9 secondary crystallographic orientations (β or θ values), for a total of 297 material orientations.

Fig. 9 Maximum Shear Stress Amplitude ($\Delta\tau_{max}$, ksi) Contour Plot at the Blade Tip Critical Point

Fig. 10 Normalized HCF life (Contour Plot) at the blade tip Critical Point, as a function of primary and secondary orientation

Fig. 11 Representative stress plots for the single crystal blade attachment region

Fig. 12 HPFTP/AT first stage blade vonMises stress plot with local zoom in of the suction side upper contact region at the blade leading edge and the local coordinate system used for the contact results.

Fig. 13 Fretting/galling induced crack in the contact region (suction side, trailing edge of blade) Several arrest marks are visible. Crystal orientation: $\Delta = -6.7^{\circ}$, $\gamma = 11.3^{\circ}$, $\beta = 4.2^{\circ}$.

Fig. 14 Fretting/galling induced cracking showing multiple origins and stage II cracks (pressure side trailing edge location). Crystal orientation: $\Delta = -2^{\circ}$, $\gamma = 3^{\circ}$, $\beta = 7^{\circ}$.

Fig. 15 Contour plot of max shear stress amplitude, $\Delta\tau_{max}$ (ksi), at the critical contact location, as a function of primary (Case number) and secondary (β or θ) crystallographic orientation.

Fig. 16 Contour plot of the parameter, $\tau_{max}*(\Delta\gamma/2)$, at the critical contact location, as a function of primary (Case number) and secondary (β or θ) crystallographic orientation.

Fig. 17 Contour plot of the parameter, $\sigma_{max}*(\Delta\varepsilon/2)$, at the critical contact location, as a function of primary (Case number) and secondary (β or θ) crystallographic orientation.

Fig. 18 Case = 0, $\beta = 0$, $\mu = 0$, Contour plot of tangential surface stress, σ_X, in upper lobe, suction side, near leading edge.

LIST OF TABLES

Table 1 Slip Planes and Slip Directions in a FCC Crystal [17]

Table 2 Strain controlled LCF test data at 1200 F for 4 specimen orientations

Table 3 Maximum values of shear stress and shear strain on the slip systems and normal stress and strain values on the same planes.

Table 4 Values of crystal orientation, friction coefficient, and max tangential normal stress σ_X at the critical contact location, for the 18 FE model runs

Slip Number	Slip Plane	Slip Direction
	Octahedral Slip a/2<110>{111}	12 Primary Slip Directions
1	[1 1 1]	[1 0 -1]
2	[1 1 1]	[0 -1 1]
3	[1 1 1]	[1 -1 0]
4	[-1 1 -1]	[1 0 -1]
5	[-1 1 -1]	[1 1 0]
6	[-1 1 -1]	[0 1 1]
7	[1 -1 -1]	[1 1 0]
8	[1 -1 -1]	[0 -1 1]
9	[1 -1 -1]	[1 0 1]
10	[-1 -1 1]	[0 1 1]
11	[-1 -1 1]	[1 0 1]
12	[-1 -1 1]	[1 -1 0]
	Octahedral Slip a/2<112>{111}	12 Secondary Slip Directions
13	[1 1 1]	[-1 2 -1]
14	[1 1 1]	[2 -1 -1]
15	[1 1 1]	[-1 -1 2]
16	[-1 1 -1]	[1 2 1]
17	[-1 1 -1]	[1 -1 -2]
18	[-1 1 -1]	[-2 -1 1]
19	[1 -1 -1]	[-1 1 -2]
20	[1 -1 -1]	[2 1 1]
21	[1 -1 -1]	[-1 -2 1]
22	[-1 -1 1]	[-2 1 -1]
23	[-1 -1 1]	[1 -2 -1]
24	[-1 -1 1]	[1 1 2]
	Cube Slip a/2<110>{100}	6 Cube Slip Directions
25	[1 0 0]	[0 1 1]
26	[1 0 0]	[0 1 -1]
27	[0 1 0]	[1 0 1]
28	[0 1 0]	[1 0 -1]
29	[0 0 1]	[1 1 0]
30	[0 0 1]	[-1 1 0]

Table 1 Slip Planes and Slip Directions in a FCC Crystal [17]

Specimen Orientation	Max Test Strain	Min Test Strain	R Ratio	Strain Range	Cycles to Failure
<001>	.01509	.00014	0.01	.01495	1326
<001>	.0174	.0027	0.16	0.0147	1593
<001>	.0112	.0002	0.02	0.011	4414
<001>	.01202	.00008	0.01	0.0119	5673
<001>	.00891	.00018	0.02	.00873	29516
<111>	.01219	-0.006	-0.49	.01819	26
<111>	.0096	.0015	0.16	0.0081	843
<111>	.00809	.00008	0.01	.00801	1016
<111>	.006	0.0	0.0	0.006	3410
<111>	.00291	-0.00284	-0.98	.00575	7101
<111>	.00591	.00015	0.03	.00576	7356
<111>	.01205	0.00625	0.52	0.0058	7904
<213>	.01212	0.0	0.0	.01212	79
<213>	.00795	.00013	0.02	.00782	4175
<213>	.00601	.00005	0.01	.00596	34676
<213>	.006	0.0	0.0	0.006	114789
<011>	.0092	.0004	0.04	0.0088	2672
<011>	.00896	.00013	0.01	.00883	7532
<011>	.00695	.00019	0.03	.00676	30220

Table 2 Strain controlled LCF test data at 1200 F for 4 specimen orientations

γ_{max} = Max shear strain of 30 slip systems for max specimen test strain value
γ_{min} = Max shear strain of 30 slip systems for min specimen test strain value
τ_{max} = Max shear stress of 30 slip systems for max specimen test strain value
τ_{min} = Max shear stress of 30 slip systems for min specimen test strain value

Specimen Orientation	γ_{max}	γ_{min}	$\Delta\gamma/2$	ε_{max}	ε_{min}	$\Delta\varepsilon/2$	τ_{max} psi	τ_{min} psi	$\Delta\tau$ psi	σ_{max} psi	σ_{min} psi	$\Delta\sigma$ psi	Cycles to Failure
<001>	0.02	0.000185	0.0099075	0.00097	9.25E-06	0.0004804	1.10E+05	1016	1.08E+05	7.75E+04	719	7.68E+04	1326
	0.023	0.0036	0.0097	0.0015	1.78E-04	0.000661	1.26E+05	1.96E+04	1.06E+05	8.93E+04	1.39E+04	7.54E+04	1593
$\tau_{max} = \tau^{14}$	0.015	2.64E-04	0.007368	7.34E-04	1.32E-05	0.0003604	8.13E+04	1452	7.98E+04	5.75E+04	1027	5.65E+04	4414
$\gamma_{max} = \gamma^{14}$	0.016	0	0.008	7.94E-04	0	0.000397	8.73E+04	0	8.73E+04	6.17E+04	0	6.17E+04	5673
	0.012	0	0.006	5.89E-04	0	0.0002945	6.47E+04	0	6.47E+04	4.57E+04	0	4.57E+04	29516
<111>	0.014	-7.06E-03	0.01053	2.05E-03	-1.01E-03	0.00153	2.25E+05	-1.10E+05	3.35E+05	1.59E+05	-7.80E+04	2.37E+05	26
	0.011	0.00176	0.00462	0.0016	0.00025	0.000675	1.77E+05	2.77E+04	1.49E+05	1.25E+05	1.96E+04	1.05E+05	843
$\tau_{max} = \tau^{25}$	.0095	9.40E-05	0.004703	0.00136	1.34E-05	0.0006733	1.49E+05	1478	1.48E+05	1.06E+05	1045	1.05E+05	1016
$\gamma_{max} = \gamma^{25}$	.0076	0	0.0038	0.001	0	0.0005	1.10E+05	0	1.10E+05	7.84E+04	0	7.84E+04	3410
	.0034	-0.0033	0.00335	0.00049	-0.00048	0.000485	5.40E+04	-5.30E+04	1.07E+05	3.80E+04	-3.70E+04	7.50E+04	7101
	.0069	1.76E-04	0.003362	9.90E-04	2.50E-05	0.0004825	1.09E+05	2771	1.06E+05	7.70E+04	1959	7.50E+04	7356
	0.014	0.007	0.0035	0.002	0.001	0.0005	2.25E+05	1.10E+05	1.15E+05	1.60E+05	7.80E+04	8.20E+04	7904
<213>	0.018	0	0.009	0.002	0	0.001	1.60E+05	0	1.60E+05	1.30E+05	0	1.30E+05	79
	0.012	1.90E-04	0.005905	0.0013	2.10E-05	0.0006395	1.06E+05	1732	1.04E+05	8.60E+04	1400	8.46E+04	4175
$\tau_{max} = \tau^{29}$	.0088	0	0.0044	0.00098	0	0.00049	8.00E+04	0	8.00E+04	6.50E+04	0	6.50E+04	34676
$\gamma_{max} = \gamma^{29}$	.0088	0	0.0044	0.00098	0	0.00049	8.00E+04	0	8.00E+04	6.50E+04	0	6.50E+04	114789
<011>	0.015	6.50E-04	0.007175	0.0039	1.68E-04	0.001866	1.23E+05	5333	1.18E+05	1.73E+05	7538	1.65E+05	2672
$\tau_{max} = \tau^{15}$	0.015	0	0.0075	0.0039	0	0.00195	1.23E+05	0	1.23E+05	1.70E+05	0	1.70E+05	7532
$\gamma_{max} = \gamma^{15}$	0.011	3.10E-04	0.005345	0.0029	8.00E-05	0.00141	9.30E+04	2532	9.05E+04	1.31E+05	3581	1.27E+05	30220

Table 3 Maximum values of shear stress and shear strain on the slip systems and normal stress and strain values on the same planes.

Primary Orientation **Case Number**	Secondary Orientation β, deg	Friction Coefficient μ	Max σ_X (Tangential normal stress, ksi)
0 (Δ=0, γ=0)	0	0.0	99.4
0	0	0.3	106.8
0	0	0.7	116.9
0	50	0.0	103.9
0	50	0.3	109.9
0	50	0.7	118.2
5 (Δ=0, γ=7.5)	0	0.0	105.7
5	0	0.3	113.1
5	0	0.7	123.3
5	50	0.0	108.6
5	50	0.3	114.4
5	50	0.7	122.6
30 (Δ=5.74, γ=-13.86)	0	0.0	84.3 (min)
30	0	0.3	89.9 (min)
30	0	0.7	97.7 (min)
30	50	0.0	94.1
30	50	0.3	98.8
30	50	0.7	105.2

Table 4 Values of crystal orientation, friction coefficient, and max tangential normal stress σ_X at the critical contact location, for the 18 FE model runs

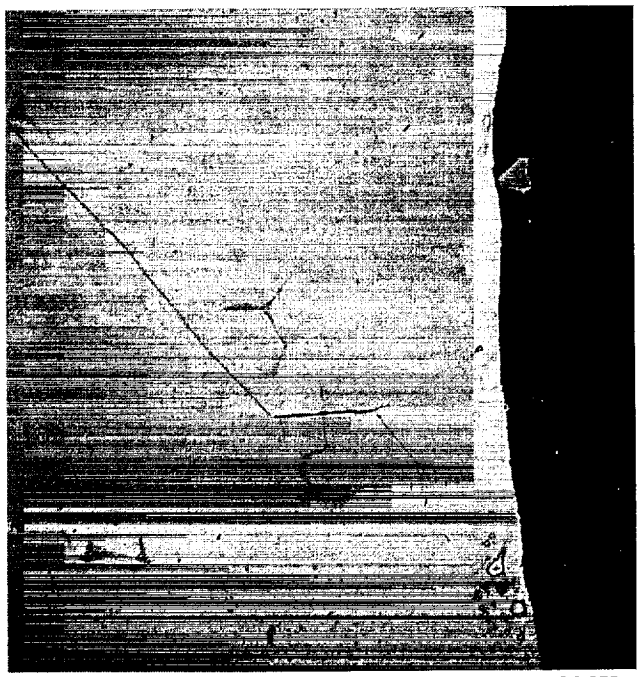

320X

Fig. 1 A subsurface fretting fatigue crack emanating from a carbide in a turbine blade attachment (PWA1422) and propagating along octahedral (111) shear planes [4].

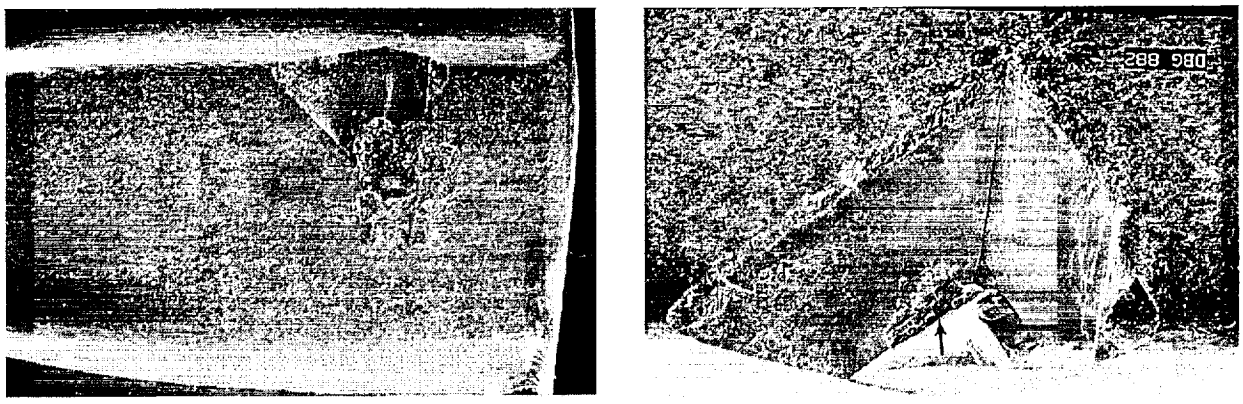

Fig. 2 Subsurface fretting fatigue crack initiation in a single crystal Ni turbine blade (platform tip) [18]

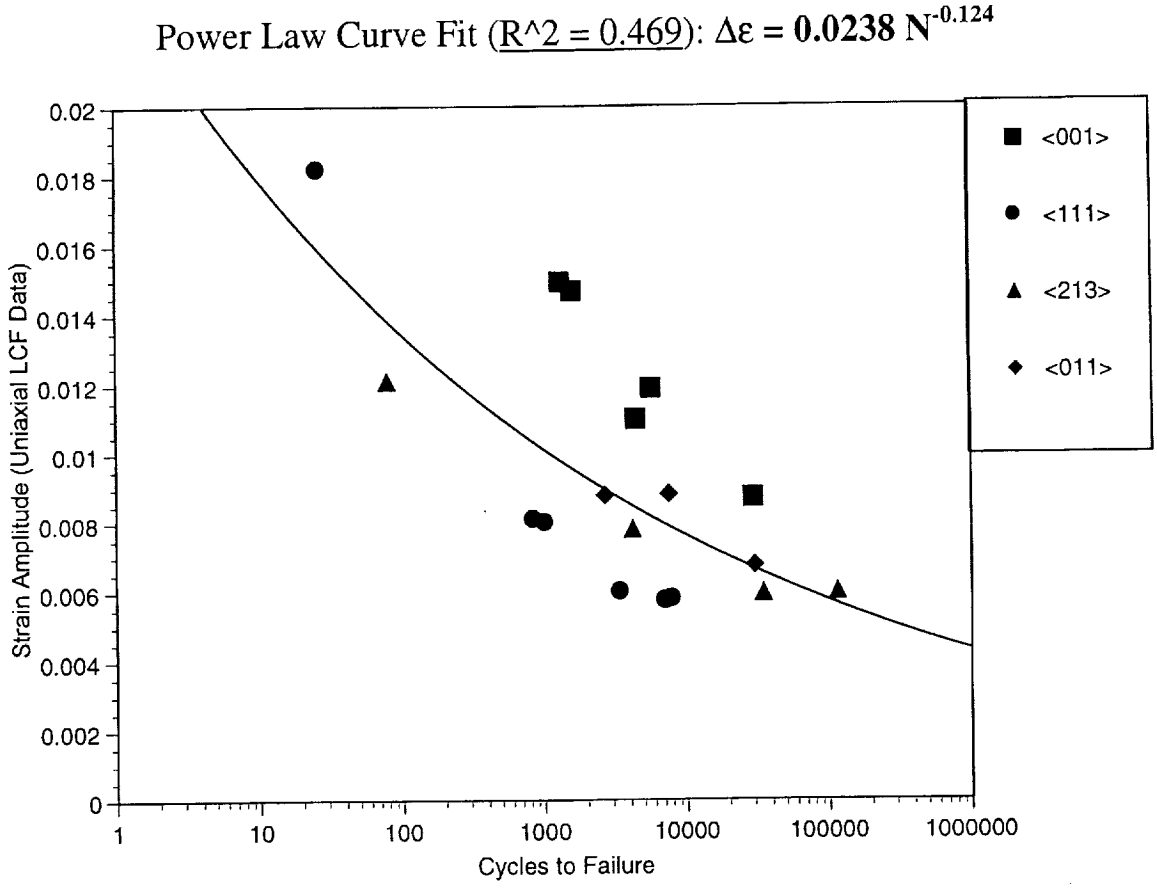

Fig. 3 Strain range Vs. Cycles to Failure for LCF test data (PWA1493 at 1200F)

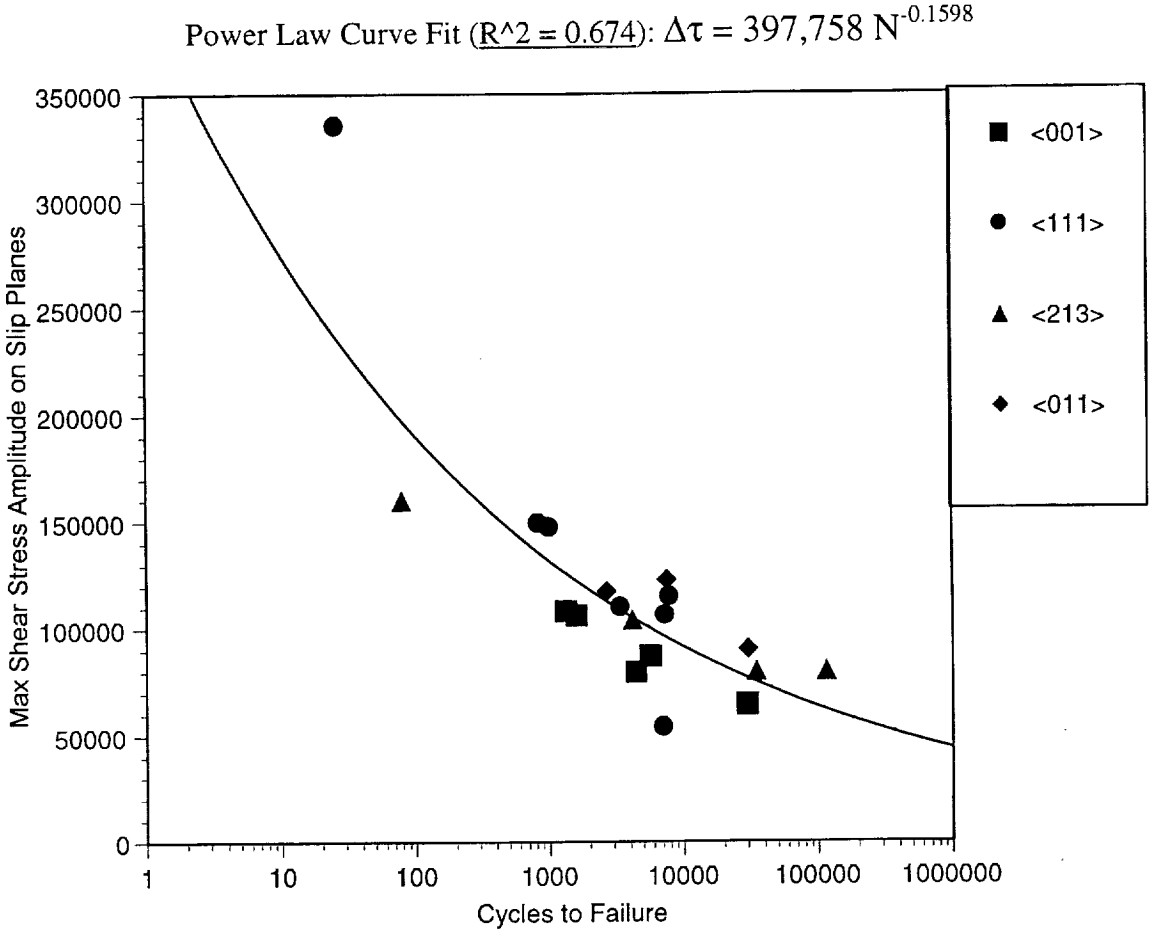

Fig. 4 Shear Stress Amplitude [$\Delta\tau_{max}$] Vs. Cycles to Failure

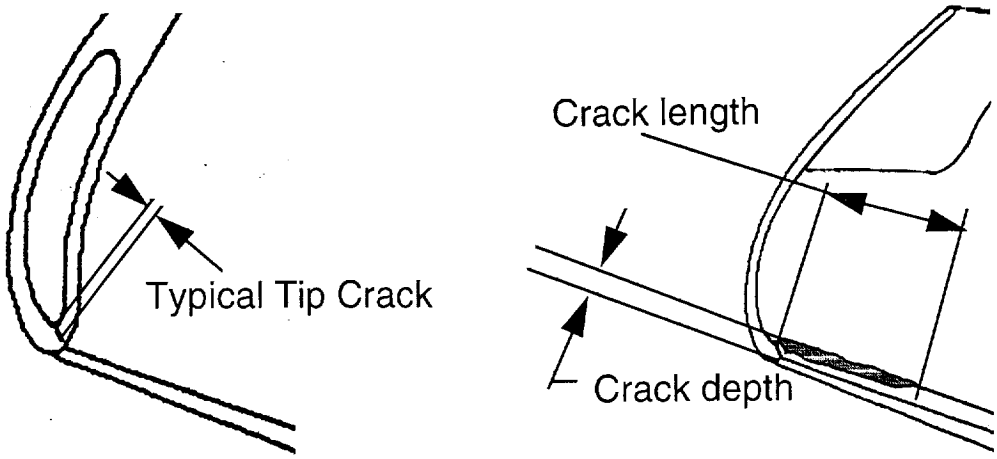

Blade leading edge crack location and orientation

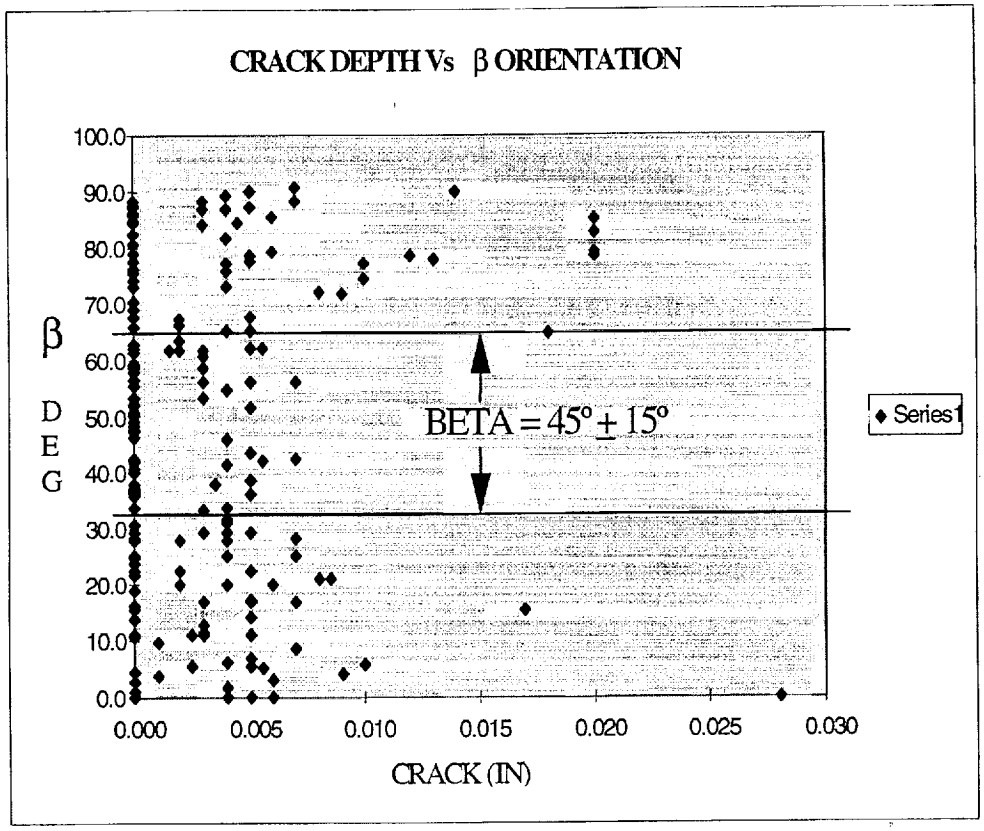

Fig. 5 Secondary Crystallographic Orientation, β, Vs Crack Depth for the SSME AHPFTP 1st Stage Turbine Blade [8, 23]

First Stage Blade Casting Coordinate System (CS 30)
Z axis along stacking axis pointing radially inward.
X axis pointing away from the pressure side.
Y axis pointing towards the second stage blade.

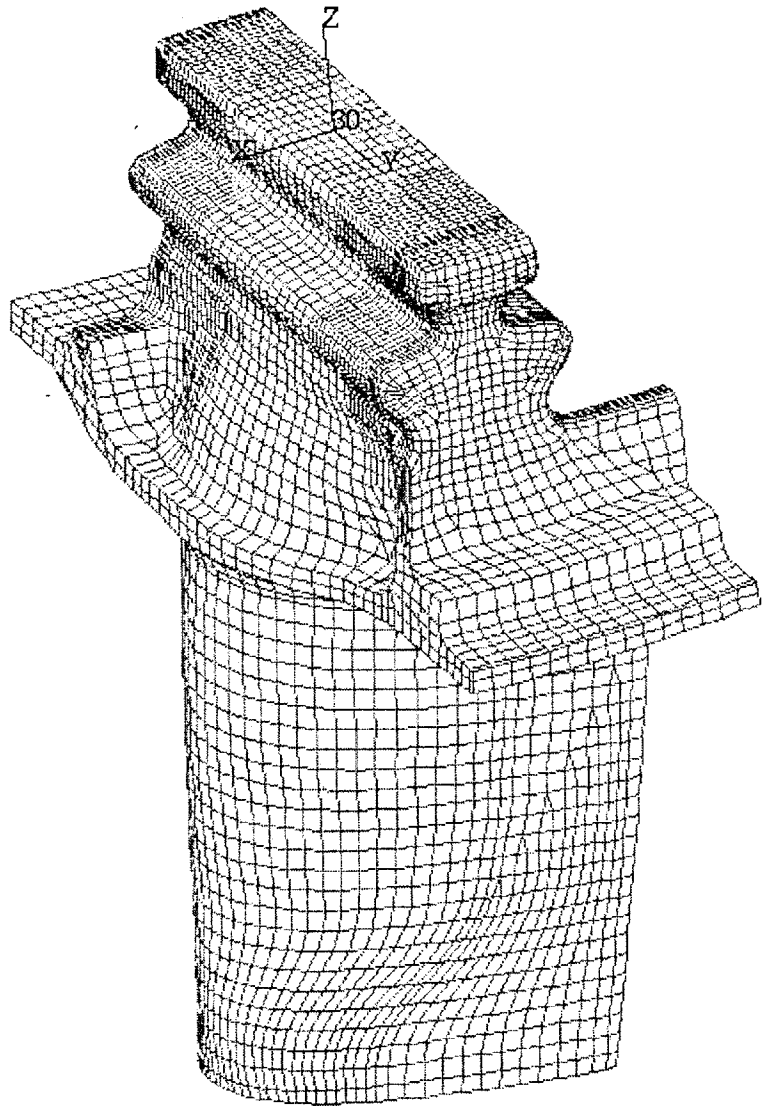

Figure 6. First Stage Turbine Blade FE Model and Casting Coordinate System

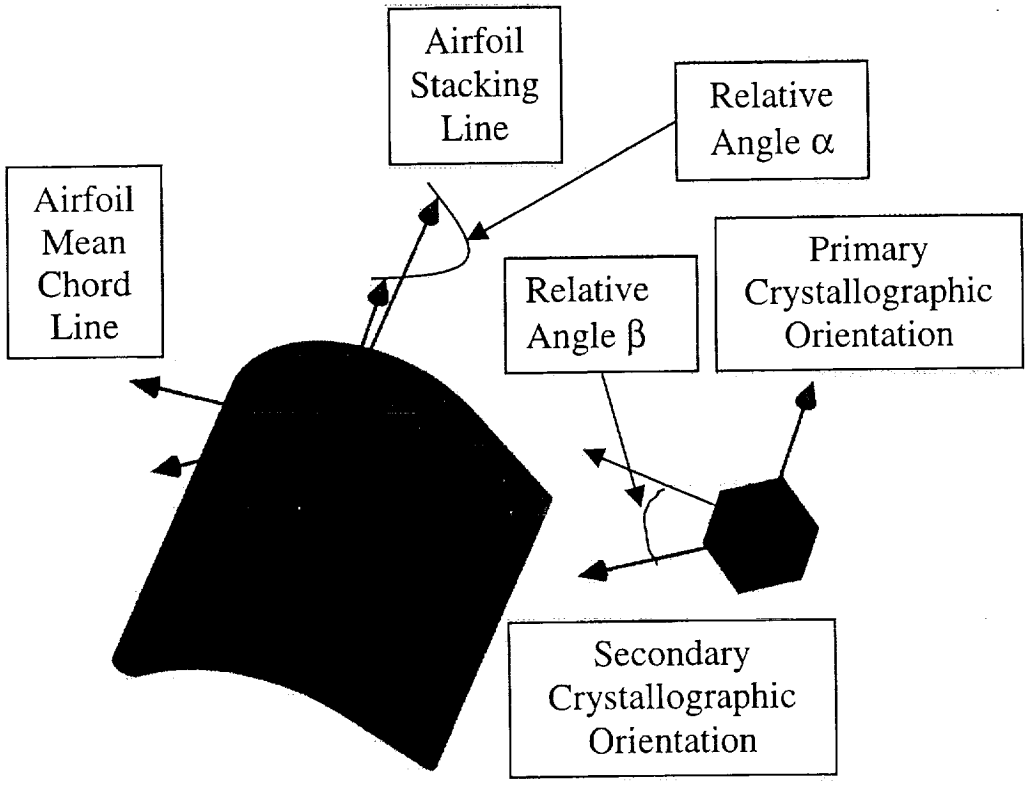

Fig. 7 Convention for Defining Crystal Orientation in Turbine Blades [8]

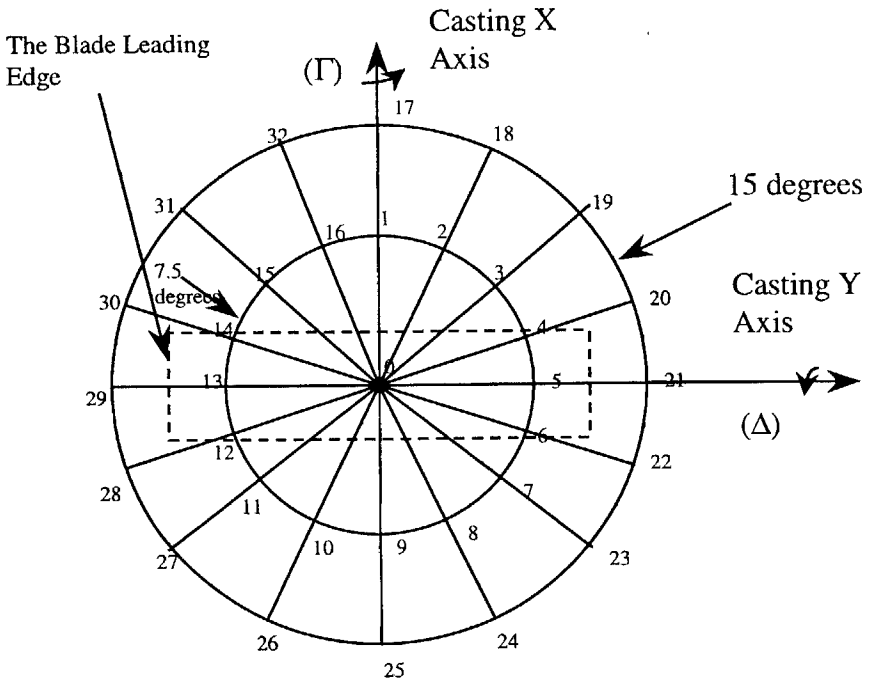

Top View of the Blade

Fig. 8 33 primary crystallographic orientations (cases) and 9 secondary crystallographic orientations (β or θ values), for a total of 297 material orientations.

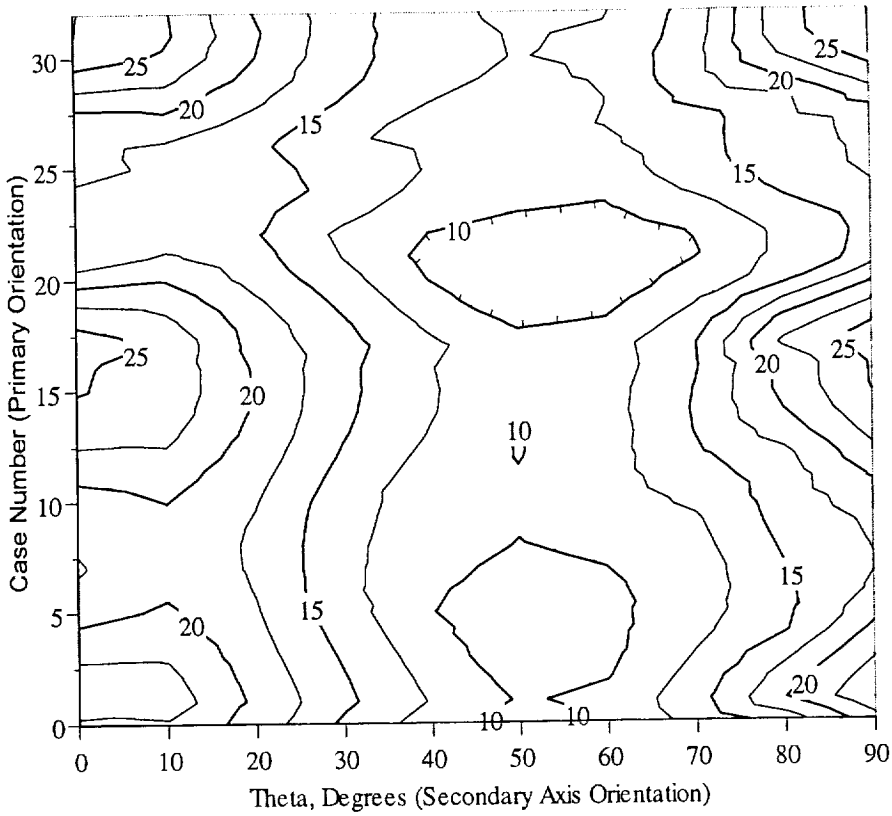

Fig. 9 Maximum Shear Stress Amplitude ($\Delta\tau_{max}$, ksi) Contour Plot at the Blade Tip Critical Point

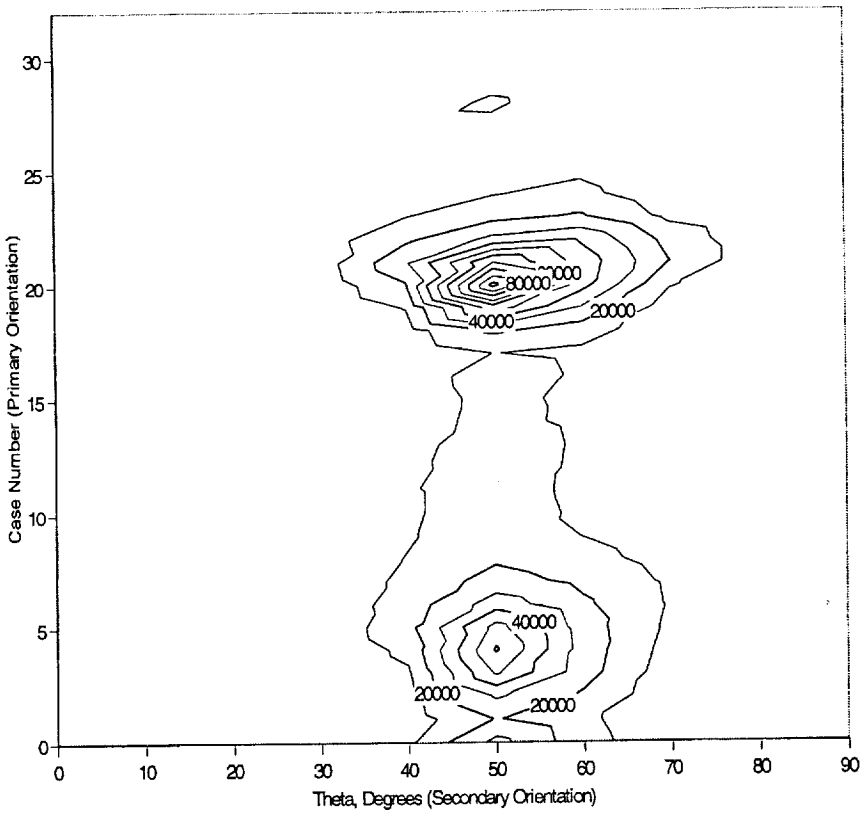

Fig. 10 Normalized HCF life (Contour Plot) at the blade tip Critical Point, as a function of primary and secondary orientation

Crystal Orientation: Case 2, 0 Primary, 22.5 Secondary, Von Mises, Suction Side

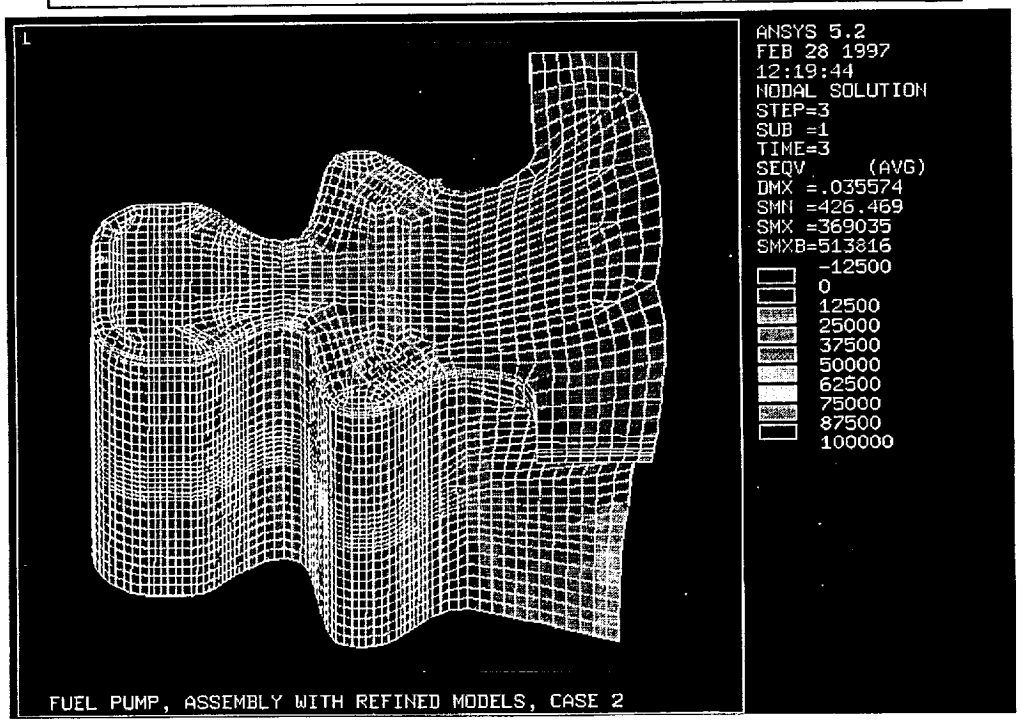

Crystal Orientation: Case 2, 0 Primary, 22.5 Secondary, Von Mises, Pressure Side

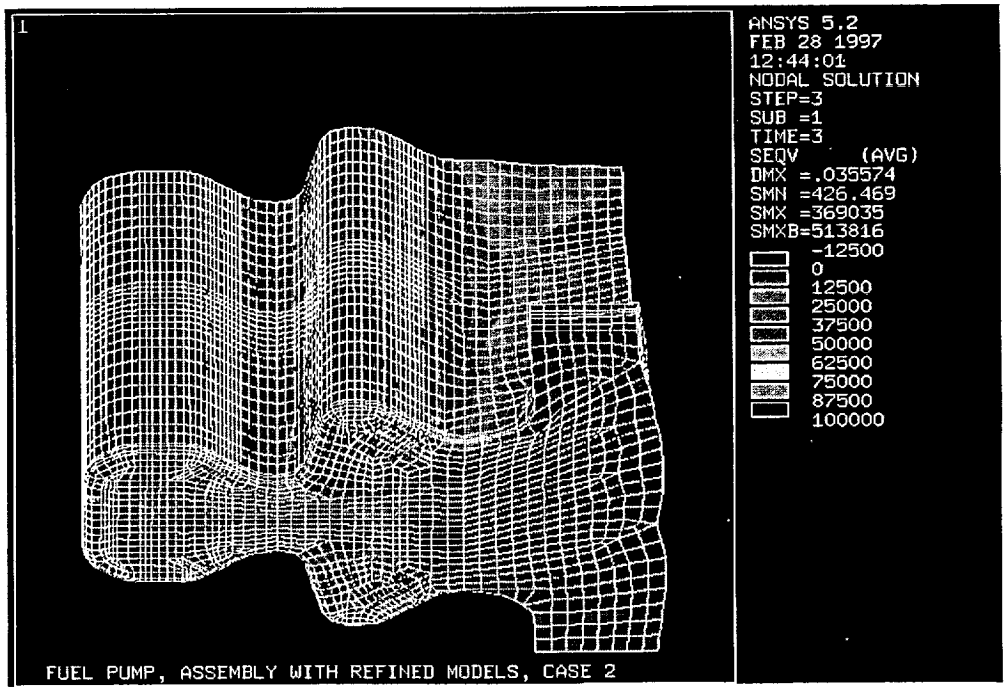

Fig. 11 Representative stress plots for the single crystal blade attachment region

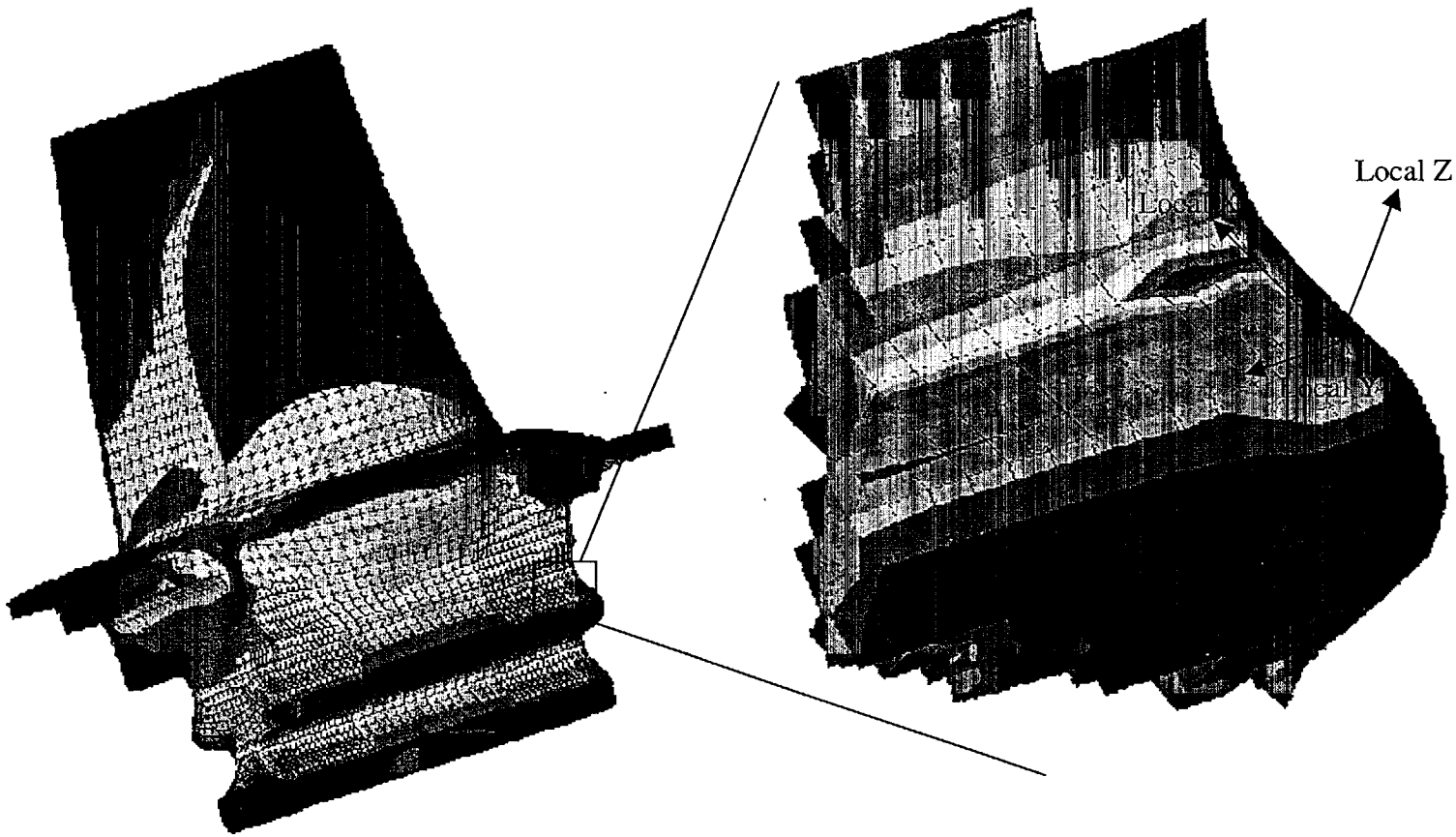

Fig. 12 HPFTP/AT first stage blade vonMises stress plot with local zoom in of the suction side upper contact region at the blade leading edge and the local coordinate system used for the contact results.

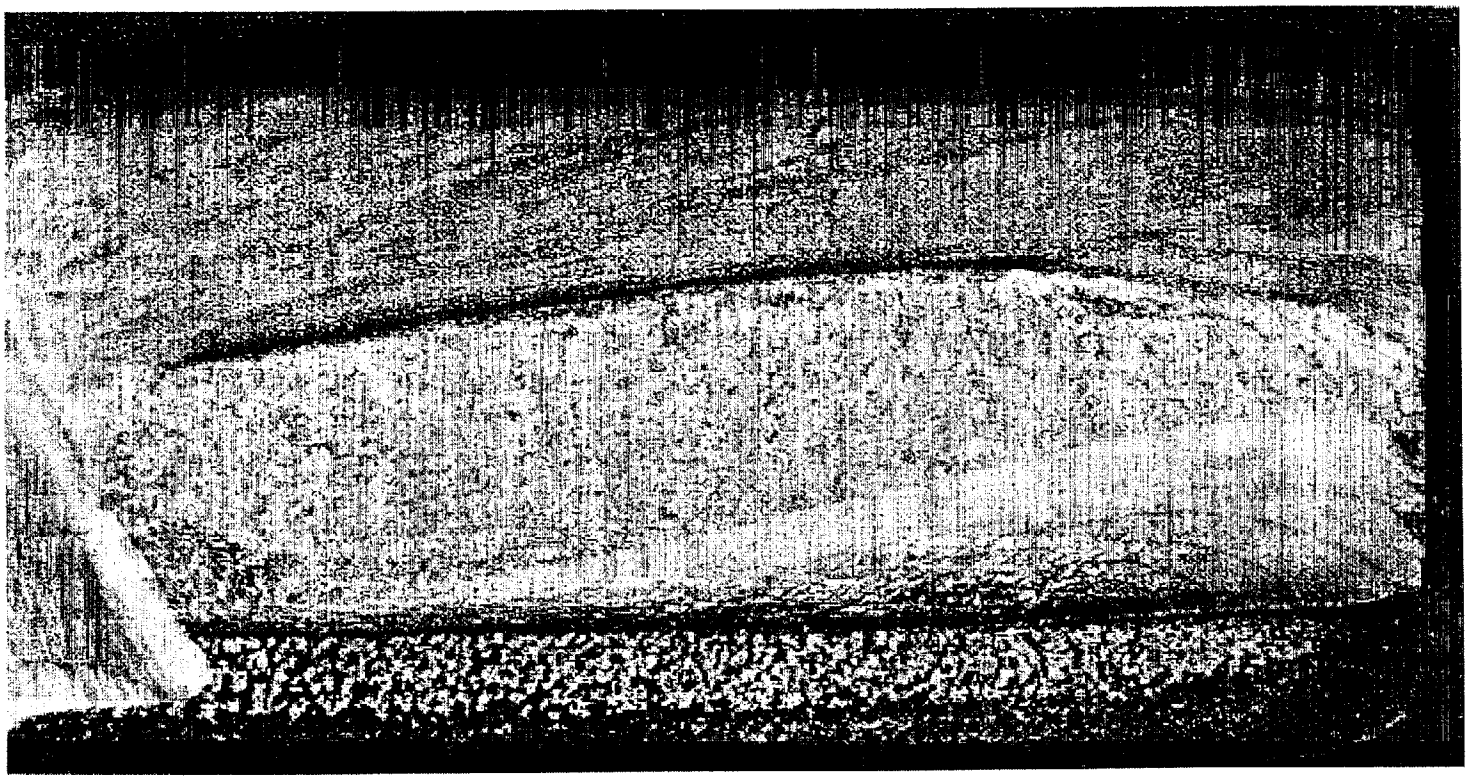

Fig. 13 Fretting/galling induced crack in the contact region (suction side, trailing edge of blade) Several arrest marks are visible. Crystal orientation: $\Delta = -6.7°$, $\gamma = 11.3°$, $\beta = 4.2°$.

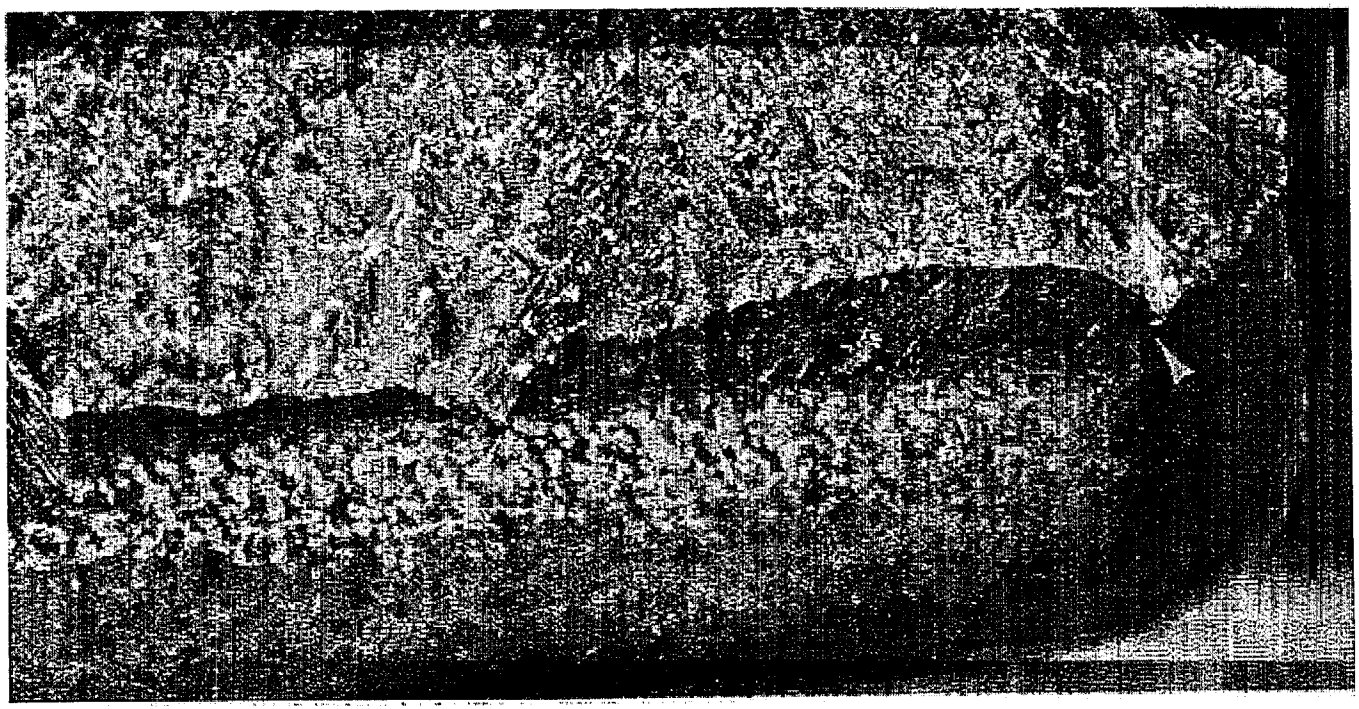

Fig. 14 Fretting/galling induced cracking showing multiple origins and stage II cracks (pressure side trailing edge location). Crystal orientation: $\Delta = -2^{o}$, $\gamma = 3^{o}$, $\beta = 7^{o}$.

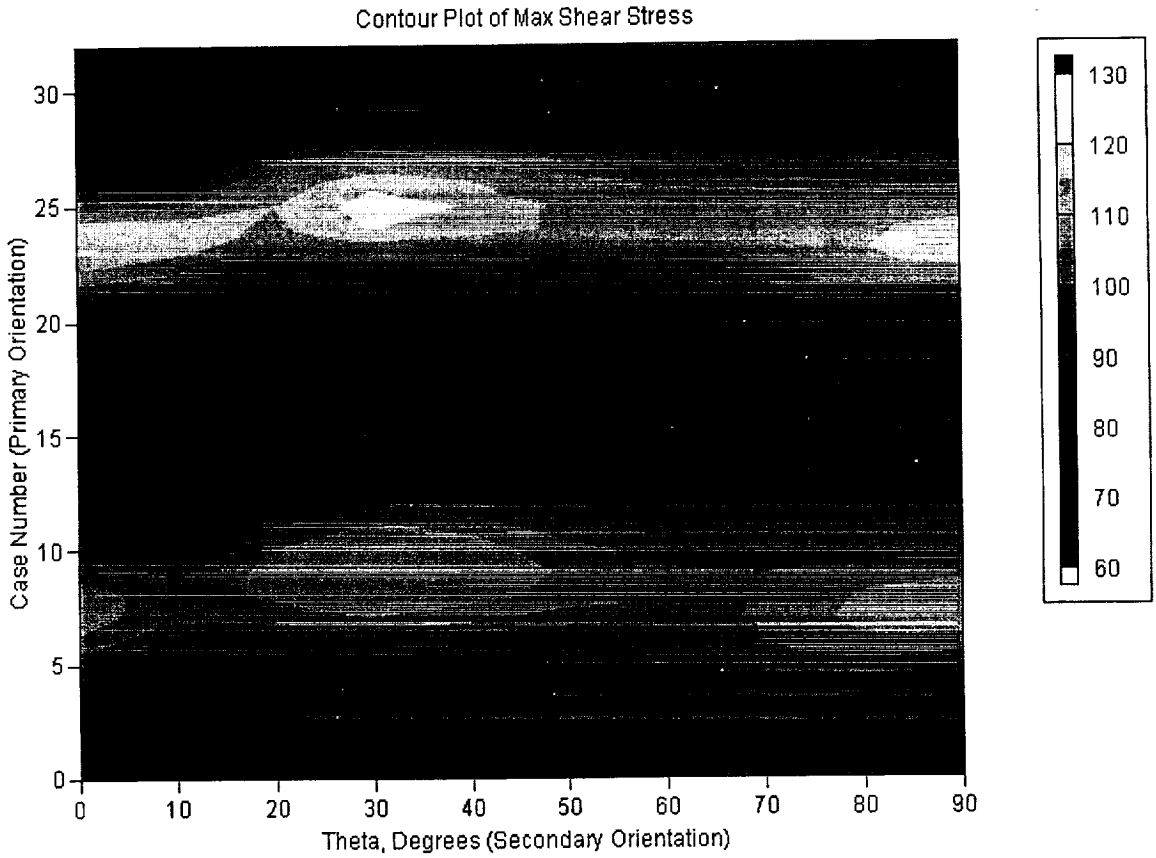

Fig. 15 Contour plot of max shear stress amplitude, $\Delta\tau_{max}$ (ksi), at the critical contact location, as a function of primary (Case number) and secondary (β or θ) crystallographic orientation.

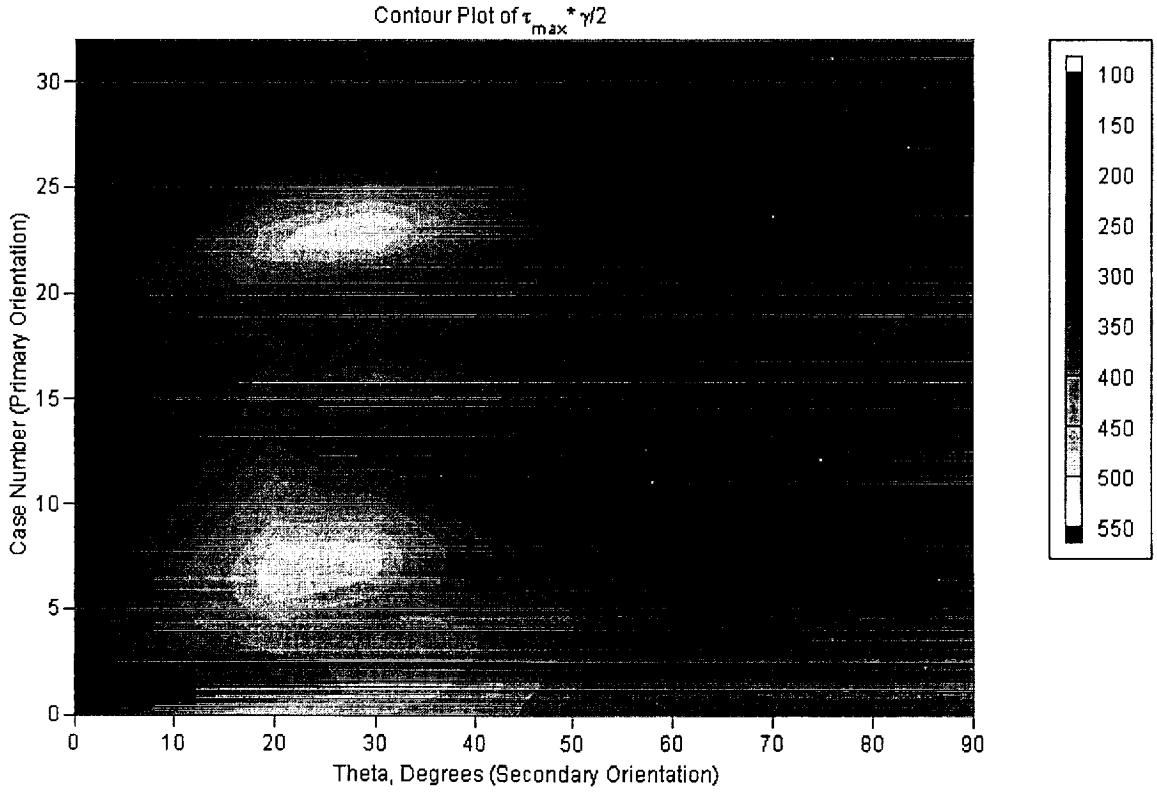

Fig. 16 Contour plot of the parameter, $\tau_{max}*(\Delta\gamma/2)$, at the critical contact location, as a function of primary (Case number) and secondary (β or θ) crystallographic orientation.

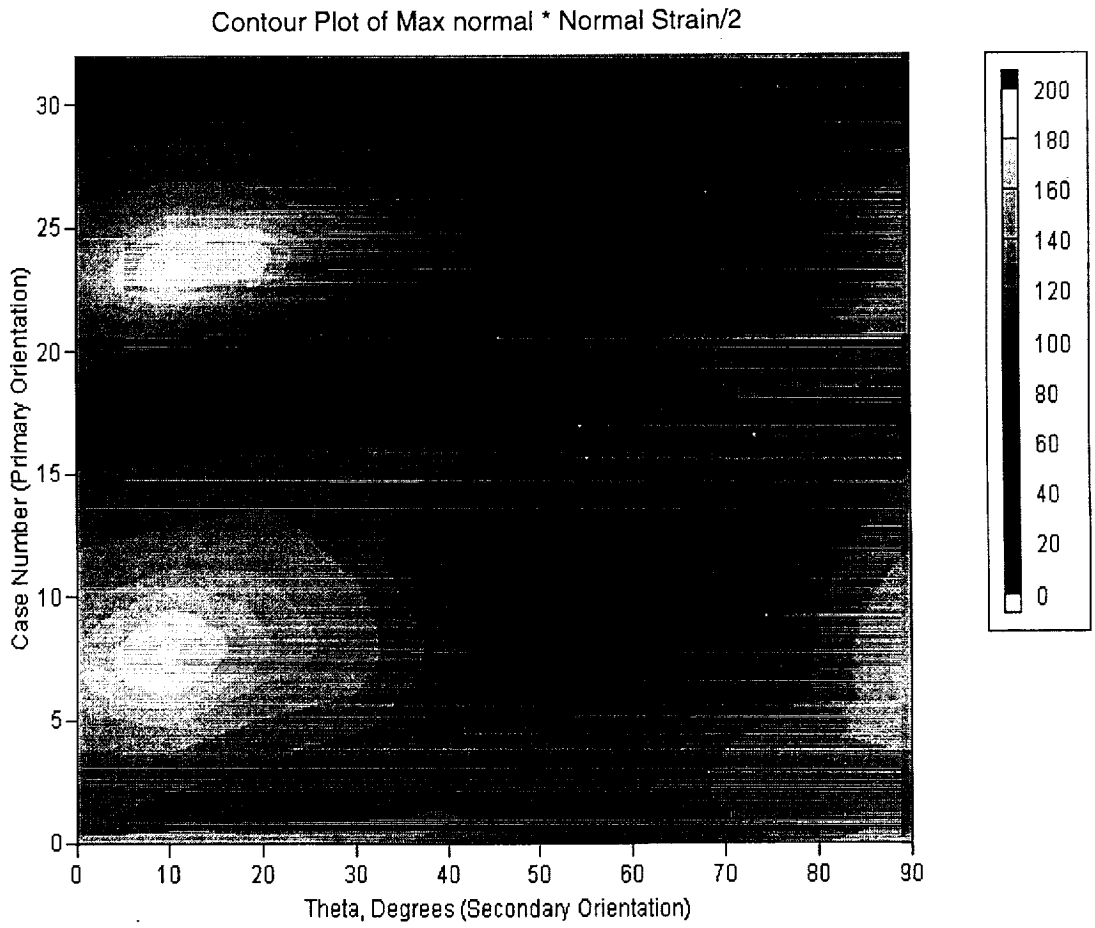

Fig. 17 Contour plot of the parameter, $\sigma_{max}*(\Delta\varepsilon/2)$, at the critical contact location, as a function of primary (Case number) and secondary (β or θ) crystallographic orientation.

Location of Maximum σ_x

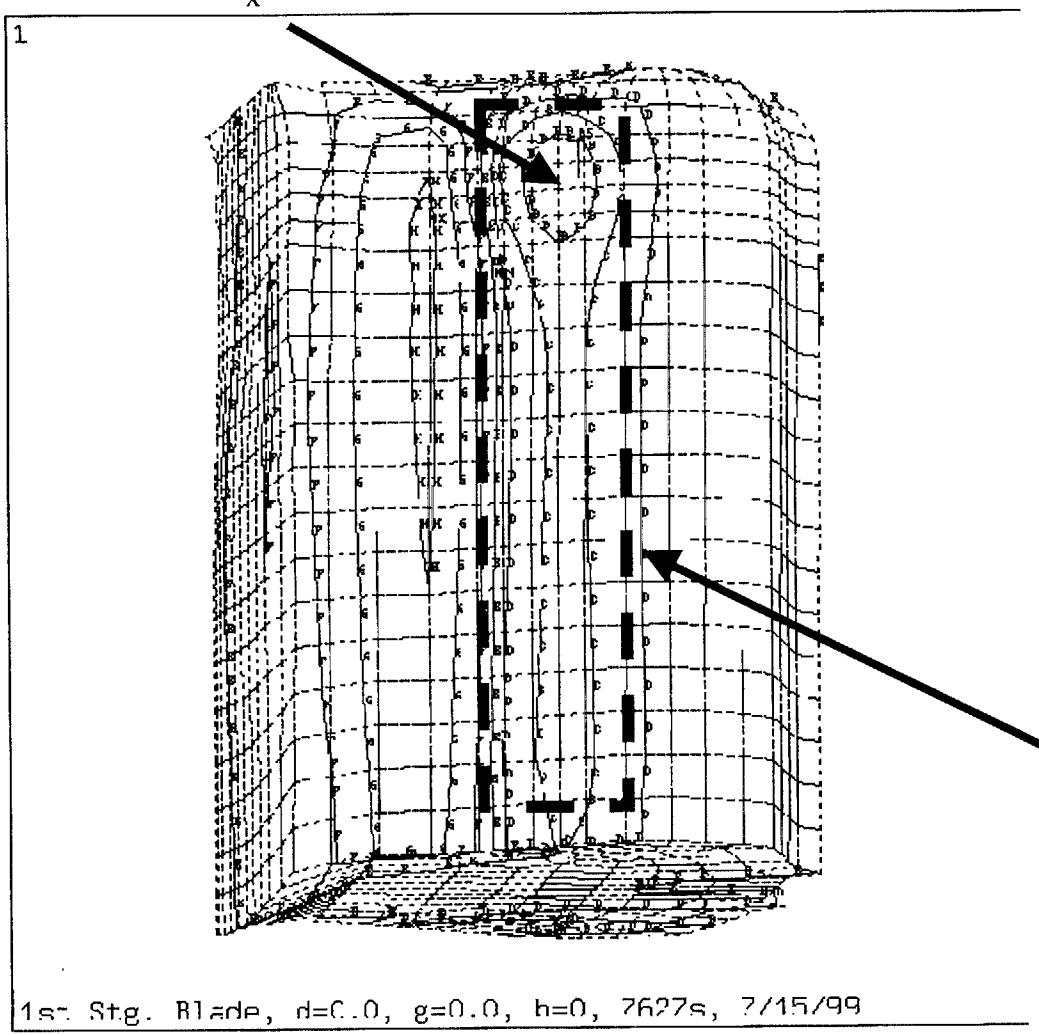

Dashed line indicates the boundary of the contact between the blade and the disc attachments, at the critical region.

Fig. 18 Case = 0, $\beta = 0$, $\mu = 0$, Contour plot of tangential surface stress, σ_x, in upper lobe, suction side, near leading edge.